TITLE:

(INVITED) Review of luminescent properties of Ce³-doped garnet phosphors: New insight into the effect of crystal and electronic structure

AUTHOR(S):

Ueda, Jumpei; Tanabe, Setsuhisa

京都大学
KYOTO UNIVERSITY

KURENAI 紅
Kyoto University Research Information Repository

ELSEVIER

Optical Materials: X

Invited Review Article

(INVITED) Review of luminescent properties of Ce^{3+}-doped garnet phosphors: New insight into the effect of crystal and electronic structure

Check for updates

Jumpei Ueda*, Setsuhisa Tanabe

Graduate School of Kyoto University, Human and Environmental Studies, Kyoto, 606-8501, Japan

ABSTRACT

The absorption and luminescence properties (centroid shift and crystal field splitting of $5d$ orbitals) of Ce^{3+}-doped garnets are summarized from the viewpoints of chemical composition (electron negativity and optical basicity) and the local crystal structure of the Ce^{3+} ion (bond length and distortion). Clear trends exist between (1) the centroid shift of $5d$ energy (ε_c) and the optical basicity of the host garnets and between (2) the crystal field splitting of the lowest $5d_1$-$5d_2$ levels (Δ_{12}) and a new distortion parameter obtained from the crystal structure data. The data of quantum yield and quenching temperatures of Ce^{3+}-doped garnets are also considered, indicating the thermal ionization process as the main mechanisms for the quenching process. Based on our recent experimental results, to prove the thermal ionization process, the principle and the most important features of the photocurrent excitation (PCE) and thermoluminescence excitation (TLE) spectra measurements are summarized. Finally, a general trend for the quenching temperature of Ce^{3+} luminescence in the garnets is discussed in terms of the energy gap between the lowest $5d_1$ level and the conduction band bottom obtained from the vacuum referred binding energy (VRBE) diagram.

1. Introduction

The series of Ce^{3+}-doped garnet luminescent materials with $5d$-$4f$ emission is a fascinating group of compounds from the viewpoints of optical application and scientific interest. The first Ce^{3+}-doped garnet optical material was developed by Blasse and Bril by using $Y_3Al_5O_{12}$ (YAG) host for the flyingspot cathode-ray tube application in 1967 [1]. After that, in the 1970s, the Ce^{3+}-doped garnets were also applied for electron detection in the scanning electron microscopes (SEM) [2]. In the 1990s, other applications using Ce^{3+}-doped garnet phosphors such as in the scintillator field for detection of X-ray and γ-ray [3–5] and in the white light emitting diode (wLED) [6–8] have been established. Recently, new optical applications such as the wavelength converter for the solar cell [9] and the persistent luminescent materials for luminous paints [10,11] and an AC-driven w-LED [12–14], are also studied and explored. The Ce^{3+}-doped garnets were used in the various application areas because of the tunability and specificity of the Ce^{3+} luminescent properties. The garnet crystal is composed of three different cation sites which accommodate many types of cations with different ionic radius. Thus, the garnet compounds have a quite wide solid solution range, which finally yields variety and tunability for physical properties as well as optical properties. In addition, the Ce^{3+}-doped garnets show many unique advantages [15,16], which is not observed in general Ce^{3+}-doped phosphors, such as high quantum efficiency (> 95%) [8], high light yield (~a few tenths thousand photons/MeV) [17–20], short lifetime (~50ns) [21], high quenching temperature (> 800K) [21–23],

large red shifting of $5d$ energy by strong crystal field splitting [24], luminescent color variation (bluish green to red) [15,25] and so on.

Among their various optical applications, the most successful one for the Ce^{3+}-doped garnets is in wLED devices. Nowadays, the wLEDs are rapidly replacing the incandescent lamps and (compact) fluorescent tubes in all lighting markets (consumer, automotive and professional) and the market is still growing. The most widely used type of wLEDs is a phosphor converted wLED, which is composed of an InGaN-based blue LED and visible luminescent inorganic phosphors, such as oxides and nitrides doped with Ce^{3+} or Eu^{2+} as an active center [6,26,27]. Since the discovery of the pre-known YAG:Ce^{3+} [1] as an excellent LED-phosphor, many alternative phosphors have been designed [28–31] but still, owing to the excellent spectral conversion characteristics, high stability under the extremely high photon flux and at high operating temperature, the YAG:Ce^{3+} as well as other Ce^{3+}-doped garnets are used in most wLEDs, which can be observed as a yellowish powder on top of the LED-chip.

On the other hand, from the fundamental point of view, unsolved mysteries for the $5d$ energy positions and the quenching process in the series of Ce^{3+}-doped garnet phosphors still remains or had remained until recently. The first biggest concerns are the exceptionally strong crystal filed splitting compared with other compounds and the unusual tendency of the crystal filed splitting for the size of cation site occupied by Ce^{3+} ion. In general, the crystal field splitting defined by the energy gap between the lowest $5d$ level and highest $5d$ level increases when the cation site size for Ce^{3+} ion becomes smaller. However, for instance in
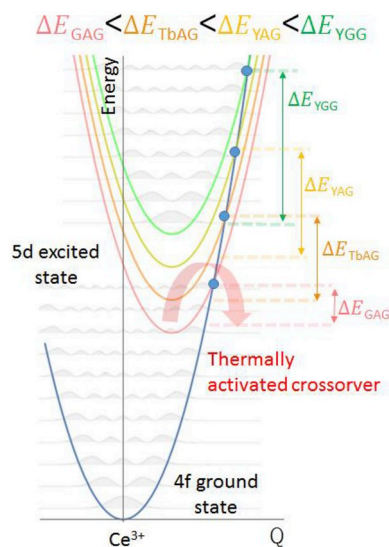
Fig. 1. Configuration coordinate diagram of Ce^{3+}-doped garnet to explain the thermally activated crossover quenching. The 5d excited states of Ce^{3+}-doped $Gd_3Al_5O_{12}$(GAG), $Tb_3Al_5O_{12}$(TbAG), $Y_3Al_5O_{12}$(YAG) and $Y_3Ga_5O_{12}$(YGG) were shown in different colors. (For interpretation of the references to color in this figure legend, the reader is referred to the Web version of this article.)

the series of $(RE)_3Al_5O_{12}$:Ce^{3+} (RE = Y, Tb, Gd), a crystal field splitting energy between the lowest $5d_1$ and second $5d_2$ level (Δ_{12}) of Ce^{3+} enlarges with increasing cation size in the order of Lu < Y < Tb < Gd [32,33]. As a result, the red-shifting of Ce^{3+} luminescence is observed even though the cation size for the Ce^{3+} site becomes larger. Here, some questions concerning the 4f-5d transitions are arising: (i) Does the centroid shift not affect the red-shift of $5d_1$? (ii) Does the large Δ_{12} yield the large crystal filed splitting (ε_{cfs}) defined by the energy gap between the lowest $5d_1$ and highest $5d_5$ levels? Also, in the garnet compounds, it is known that the distortion for the Ce^{3+} site affects the crystal field splitting [34–36]. However, complete understanding of the relationship between the local structure and the crystal filed splitting has not been reached yet, bringing to another question: (iii) Can we define a new distortion parameter to explain the crystal field splitting in the whole Ce^{3+}-doped garnets?

The second concern is related to luminescence quenching. The luminescence quenching of the 5d-4f transition was often explained by the thermally activated crossover quenching using configuration coordinate (CC) diagrams [37,38] as shown in Fig. 1. The activation barrier for the cross-over quenching decreases for a larger configurational off-set and a smaller energy difference between the states. For instance, among various Ce^{3+}-doped garnets, $Gd_3Al_5O_{12}$ (GAG) and $Tb_3Al_5O_{12}$ (TbAG) are suitable candidates as orange phosphors for warm white LEDs. By increasing the cation size of the dodecahedral site for Ce^{3+} in the order of Y < Tb < Gd, the $5d_1$ energy of Ce^{3+} decreases (red-shifting) and the quenching temperature ($T_{50\%}$) decreases [32].

Therefore, the agreement between the tendency of the thermal quenching and the estimated activation energy from the configuration coordinate diagram seems to suggest the thermal quenching is caused by the thermally activated cross-over process (Fig. 1). However, this tendency is often not followed by other garnet systems. For instance, in $Y_3Al_{5-x}Ga_xO_{12}$:Ce^{3+}, the $5d_1$ energy increases with Ga content and the activation energy of cross-over quenching is expected to be increased [39,40], but the $T_{50\%}$ decreases [41]. This fact suggested us that there are possibilities of another ionization quenching process in all the Ce^{3+}-doped garnets including even GAG and TbAG hosts.

In the following sections, we summarize the garnet crystal structure and visualize the local structure around Ce^{3+} to discuss the distortion, and then, we introduce the background of the Ce^{3+}:4f-5d transition energy, the centroid shift and crystal field splitting. Subsequently, in

Chapter 2, the energy data of five 5d energy levels collected from the literature and from new photoluminescence excitation spectra are analyzed to separate the contribution of the centroid shift and the crystal filed splitting from the red-shift of the lowest $5d_1$ energy in Ce^{3+}-doped garnets. Based on these investigations, the centroid shift energy is found to vary with the garnet composition. In addition, a clear correlation between the centroid shift and the optical basicity obtained from the garnet composition is introduced. A correlation between Δ_{12} and ε_{cfs} was found, and a new distortion parameter for the Ce^{3+} site is proposed to explain the crystal filed splitting effect on the Ce^{3+} 5d excitation state. In chapter 3, we summarize some methods to demonstrate the thermal ionization quenching process and discuss the quenching process of Ce^{3+}-doped garnets based on the experimental results and the vacuum referred binding energy (VRBE) diagram. In view of the dependence of centroid shift (ε_c) with the garnet composition, the VRBE diagrams were constructed by the new $U(6,A)$ parameters obtained from the ε_c of Ce^{3+}:5d energy. From the quenching temperature and the energy gap between $5d_1$ and the bottom of the conduction band obtained by the VRBE diagram, the thermal ionization process is suggested as the main quenching process in Ce^{3+}-doped garnets.

1.1. Garnet structure

Originally, the meaning of garnet was a group of silicate minerals, which are found in all over the world and used as a gemstone. In the natural silicate garnet minerals, it is known that there are several compositions such as $Mg_3Al_2Si_3O_{12}$ (Pyrope), $Ca_3Al_2Si_3O_{12}$ (Grossular), $Fe_3Al_2Si_3O_{12}$ (Almandite), $Mn_3Al_2Si_3O_{12}$ (Spessartine), $Mg_3Cr_2Si_3O_{12}$ (Knorringite), $Ca_3Cr_2Si_3O_{12}$ (Uvarovite), $Mg_3Fe_2Si_3O_{12}$ (Andrade) and so on. The chemical formula of general garnet crystals can be written as $\{A\}_3[B]_2(C)_3O_{12}$. The garnet crystal structure was firstly described in 1917 using Almandite by Nishikawa [42]. This work is not widely known, but he already identified that the garnet structure has a group O_h^{10} in Schonfles's notation [42]. After that, in 1929, Menzer also determined the garnet structure in several minerals [43] as $Ia\bar{3}d$ space group. Among the numerous garnet compounds, the $Y_3Al_5O_{12}$ crystal is the most famous functional garnet material for various optical applications. However, this artificial compound cannot be found in natural minerals. In 1951, Jaffe investigated the role of yttrium ions in the garnet minerals and predicted the substitution of Y^{3+}-Al^{3+} for Mn^{2+}-Si^{4+} in a $Mn_3Al_2Si_3O_{12}$ garnet [44]. In the same year, Yoder et al. also suggested that $\{Mn_{1-x}Y_x\}_3[Al]_2(Si_{1-x}Al_x)_3O_{12}$ solid solutions can be represented, and then successfully prepared the end member of $\{Y\}_3[Al]_2(Al)_3O_{12}$, which actually has a garnet structure [45]. Nowadays, it is known that there are some artificial garnets with compositions such as aluminate, gallate and germanate garnets beyond the natural silicate minerals.

Fig. 2a shows the unit cell of the general cubic garnet structure of $\{A\}_3[B]_2(C)_3O_{12}$ oxide garnet. The space group is $Ia\bar{3}d$ (No.230). The lattice constant (a_0) is generally around 12 Å. $\{A\}$ represents a cation in
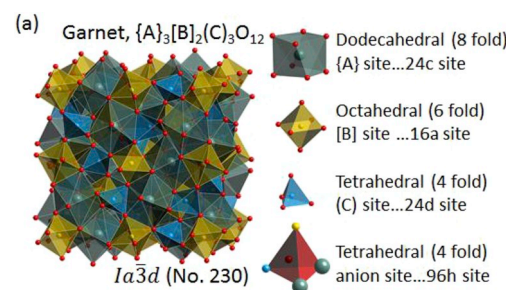

Fig. 2. (a) Unit cell of garnet structure with dodecahedron $\{A\}$ site (gray), octahedral [B] site (yellow), tetrahedral (C) site (blue) and anions (red spheres). (For interpretation of the references to color in this figure legend, the reader is referred to the Web version of this article.)
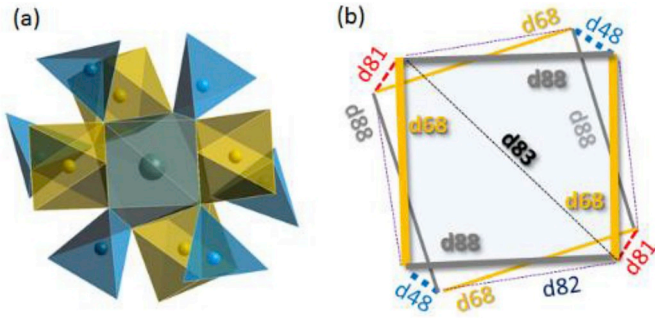
Fig. 3. (a) Local structure of dodecahedral site (four nearest dodecahedral sites are not depicted) and (b) corresponding schematic dodecahedral framework represented by sharing edges (d_{88}, d_{68}, d_{48}) and non-sharing edges(d_{81}, d_{82}, d_{83}).

the dodecahedral (8-fold) site, which is represented by 24c as Wyckoff position. [B] and (C) represent cations in octahedral (6-fold) site (16a) and in the tetrahedral (4-fold) site (24d), respectively. All the oxygen anions occupy tetrahedral sites (96 h). In the unit cell, 160 atoms exist. The dodecahedral {A} site can be occupied by Y^{3+}, Gd^{3+}, Lu^{3+}, Tb^{3+}, Ca^{2+}, Sr^{2+}, Mg^{2+}; the octahedral [B] site can be occupied by Al^{3+}, Ga^{3+}, In^{3+}, Sc^{3+}, Y^{3+}, Mg^{2+}, Fe^{3+}, Cr^{3+}; the tetrahedral (C) site can be occupied by Al^{3+}, Ga^{3+}, Si^{4+}, Ge^{4+}. The combination of cations in {A}, [B], (C) sites are varied and limited by the relationship of ionic radius and valence states for the net charge neutrality.

The Ce^{3+} ion, as do other Ln^{3+} ions, occupies the dodecahedral {A} site. The environment of local structures around the {A} site is important for understanding the optical properties of Ce^{3+} ion. Fig. 3a shows the cluster of the dodecahedral site with four octahedral and six tetrahedral sites. Here, the other dodecahedral sites are not shown for avoiding the complex structure. The dodecahedral {A} site shares two edges with two tetrahedral (C) sites, four edges with four octahedral [B] site and four

edges with four dodecahedral site. In addition, the dodecahedral {A} site shares four corners with a tetrahedral (C) site (totally four). As referring the naming way by Euler [46], the shared edges between tetrahedral and dodecahedral sites, between octahedral and dodecahedral sites and between dodecahedral and dodecahedral sites are expressed as d_{48}, d_{68}, d_{88}, respectively. Three different un-shared edges are represented as d_{81}, d_{82} and d_{83} [47]. Fig. 3b shows the schematic dodecahedral site expressed by the defined edges. Totally, the dodecahedral site possesses 18 edges of $2 \times d_{48}$, $4 \times d_{68}$, $4 \times d_{88}$, $2 \times d_{81}$, $4 \times d_{82}$, $2 \times d_{83}$. The bond lengths between the {A} cation and O^{2-} and between O^{2-} and O^{2-} that create an edge of the dodecahedral site are closely related to the optical properties of Ce^{3+} ion. The distortion factor is often estimated by the ratio of dodecahedral edges. Wu et al. proposed the distortion parameter by the ratio of d_{88} with respect to d_{81} to explain the unusual tendency of luminescence wavelength in some specific garnet composition [34]. However, we find the d_{88}/d_{81} is not a perfect parameter if we extended this parameter to whole garnet compositions, and propose that d_{83}/d_{48} divided by the modified average bond length between the {A} cation and O^{2-} anion is a reasonable parameter to discuss the distortion as discussed later in chapter 2.

1.2. Ce^{3+}:4f-5d transition

Ce^{3+} ion is one of the lanthanide ions (atomic number: 58) and it is characterized by the electronic configuration of $[Xe]4f^1$. From the Dieke diagram, it is known that Ce^{3+} ion with $[Xe]4f^1$ electronic configuration has one 4f-4f absorption due to the transition from $^2F_{5/2}$ to $^2F_{7/2}$ levels, which are generated by the spin-orbit coupling. In addition, Ce^{3+} ion can be excited into $[Xe]4f^05d^1$ electronic configuration. In the free ion, the absorption from the 4f ground state to the 5d excited state of $[Xe]4f^05d^1$ can be observed at around 6 eV [48,49]. The 5d excited state is split by the spin-orbit coupling into $^2D_{3/2}$ and $^2D_{5/2}$, the absorption energies between $^2F_{5/2}$ and $^2D_{3/2}$ and between $^2F_{5/2}$ and the average energy of $^2D_{3/2}$ and $^2D_{5/2}$ are 6.12 and 6.35 eV, respectively, in the free ion of Ce^{3+}
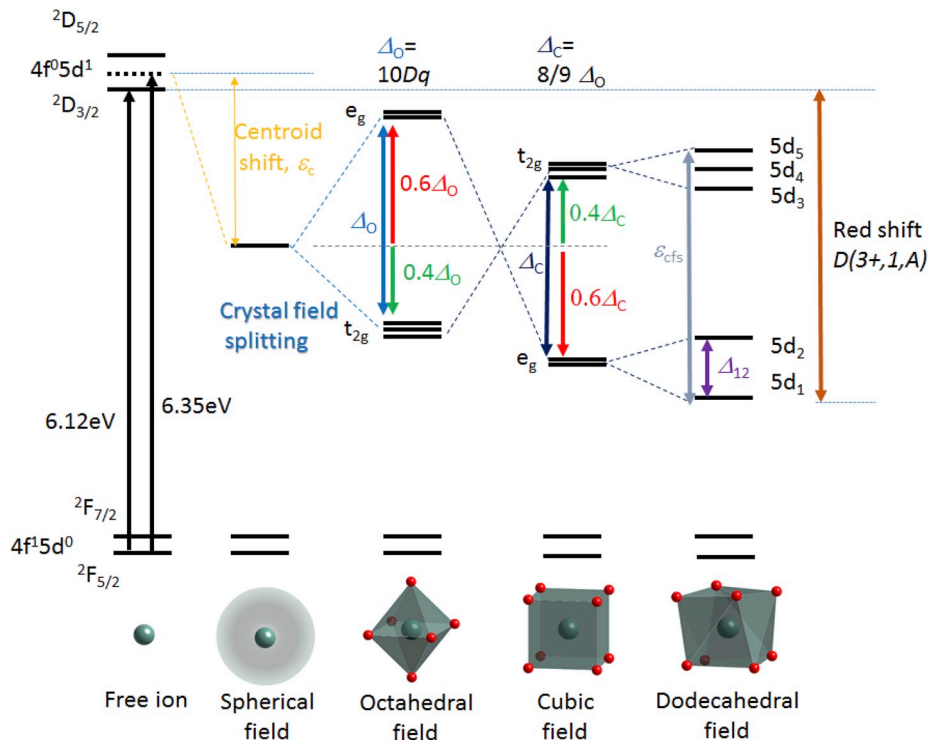

Fig. 4. Schematic energy diagram of Ce^{3+} ion in the free ion state, spherical field, octahedral field, cubic field and dodecahedral field for understanding the centroid shift and the crystal filed splitting.

Table 1
Collected spectroscopic data of $5d_1$, $5d_2$ excitation bands and $D(1,3+,A)$ of Ce^{3+} ion and structural data of R_{av}, d_{88}, d_{48}, d_{81}, d_{83} and lattice constant of garnet hosts.

	$5d_2$ (nm)	$5d_1$ (nm)	$D(1,3+,A)$ (eV)	Ref.	R_{av} (pm)	d_{88} (Å)	d_{48} (Å)	d_{81} (Å)	d_{83} (Å)	Ref.	Lattice constant (Å)	Ref.
$Gd_3Al_5O_{12}$	337	470	3.48	[25,55]	249	3.006	2.692	2.963	4.122	[56]	12.11	[56]
$Gd_3Al_4Ga_1O_{12}$	339	459	3.42	[25]							12.17	[57]
$Gd_3Al_3Ga_2O_{12}$	340	448	3.35	[25]	252	3.071	2.76	2.97	4.166	[56]	12.22	[57]
$Gd_3Al_2Ga_3O_{12}$	344	441	3.31	[25]	252	3.049	2.813	2.926	4.134	[56]	12.27	[57]
$Gd_3Al_1Ga_4O_{12}$	347	437	3.28	[25]							12.32	[57]
$Gd_3Ga_5O_{12}$	348	428	3.22	[25]	249	2.947	2.798	3.083	4.046	[56]	12.38	[56]
$Gd_2Y_1Al_5O_{12}$	337	467	3.47	[57]							12.13	[57]
$Gd_2Y_1Al_4Ga_1O_{12}$	339	456	3.4	[57]							12.18	[57]
$Gd_2Y_1Al_3Ga_2O_{12}$	343	447	3.34	[57]							12.21	[57]
$Gd_2Y_1Al_2Ga_3O_{12}$	345	442	3.32	[57]							12.23	[57]
$Gd_2Y_1Al_1Ga_4O_{12}$	347	440	3.3	[57]							12.29	[57]
$Gd_1Y_2Al_5O_{12}$	339	463	3.44	[57]							12.04	[57]
$Gd_1Y_2Al_4Ga_1O_{12}$	341	453	3.38	[57]							12.09	[57]
$Gd_1Y_2Al_3Ga_2O_{12}$	344	441	3.31	[57]							12.15	[57]
$Gd_1Y_2Al_2Ga_3O_{12}$	348	439	3.3	[57]							12.2	[57]
$Gd_1Y_2Al_1Ga_4O_{12}$	349	437	3.28	[57]							12.26	[57]
$Y_3Al_5O_{12}$	340	457	3.41	[25,58]	245	2.859	2.701	2.899	3.962	[59]	12.01	[59]
$Y_3Al_4Ga_1O_{12}$	346	454	3.39	[25]	245	2.856	2.694	2.973	3.956	[59]	12.04	[59]
$Y_3Al_3Ga_2O_{12}$	347	446	3.34	[25]	245	2.83	2.738	2.925	3.931	[59]	12.09	[59]
$Y_3Al_2Ga_3O_{12}$	349	435	3.27	[25]	245	2.826	2.754	2.981	3.922	[59]	12.16	[59]
$Y_3Al_1Ga_4O_{12}$	355	430	3.24	[25]	246	2.811	2.78	2.966	3.914	[59]	12.21	[59]
$Y_3Ga_5O_{12}$	350	416	3.14	[25]	246	2.816	2.812	2.976	3.913	[47]	12.27	[47]
$Lu_3Al_5O_{12}$	348	448	3.35	[25]	243	2.75	2.684	2.877	3.85	[46]	11.91	[46]
$Lu_3Al_4Ga_1O_{12}$	[350]	438	3.29	[25]							11.97	
$Lu_3Al_3Ga_2O_{12}$	[348]	432	3.25	[25]							12.05	
$Lu_3Al_2Ga_3O_{12}$	[350]	428	3.22	[25]							12.09	
$Lu_3Al_1Ga_4O_{12}$	[358]	415	3.13	[25]							12.15	
$Lu_3Ga_5O_{12}$	[357]	408	3.08	[25]	245	2.713	2.793	2.959	3.812	[46]	12.19	
$Y_3Sc_2Al_3O_{12}$	348	443	3.32	[60,61]	246	2.745	2.684	2.929	3.974	[62]	12.27	[46]
$Y_3Sc_2Al_2Ga_1O_{12}$	349	427	3.22	[60,61]							12.39	[60]
$Y_3Sc_2Al_1Ga_2O_{12}$	350	420	3.17	[60,61]							12.43	[60]
$Y_3Sc_2Ga_3O_{12}$	357	419	3.16	[60,61]	248	2.772	2.8	2.987	3.949	[63]	12.45	[60]
$Gd_3Sc_2Al_3O_{12}$	341	457	3.41	[60,61]	247	2.815	2.705	2.954	4.053	[64]	12.39	[64]
$Lu_{1.5}Y_{1.5}Al_5O_{12}$	343	453	3.38	This work								
$Y_{2.5}La_{0.5}Al_5O_{12}$	342	462	3.44	[65]								
$Tb_3Al_5O_{12}$	338	465	3.45	[66,67]	244	2.889	2.728	2.911	3.962	[68]	12.00	[68]
$Sr_3Y_2Ge_3O_{12}$	297	433	3.26	[69,70]	255	3.083	2.738	3.071	4.491	[71]	13.09	[69]
$Sr_3Lu_2Ge_3O_{12}$	[300]	435	3.27	[69,70]								
$Ca_3Y_2Ge_3O_{12}$	312	425	3.2	[69]	253	2.867	2.705	2.969	4.259	[72]	12.81	[69]
$Ca_3Lu_2Ge_3O_{12}$	312	421	3.17	[69]								[69]
$Ca_3Sc_2Si_3O_{12}$	308	432	3.25	[23]	247	2.921	2.548	2.891	4.239	[73]	12.25	[73]
$Mg_3Y_2Ge_3O_{12}$	320	463	3.44	[74]	249	2.748	2.677	2.929	3.973	[72]	12.25	[74]
$Mg_3Y_2Ge_3O_{12}$ (absorption)	323	425	3.2	[75]	249	2.748	2.677	2.929	3.973	[72]	12.25	[74]
$Mg_3Y_2Ge_{2.7}Si_{0.3}O_{12}$	318	466	3.46	[74]							12.24	[74]
$Mg_3Y_2Ge_{2.1}Si_{0.9}O_{12}$	314	468	3.47	[74]							12.19	[74]
$Mg_3Y_2Ge_{1.5}Si_{1.5}O_{12}$	310	470	3.48	[74]							12.15	[74]
$Mg_3Y_2Ge_{0.9}Si_{2.1}O_{12}$	308	474	3.5	[74]							12.11	[74]
$Lu_2Mg_2Al_2Si_2O_{12}$	327	436	3.28	[76]	250	2.866	2.624	2.755	4.027	[76]	11.88	[76]
$Lu_2Ca_1Mg_2(SiO_4)_3$	322	473	3.5	[77]	243	2.749	2.557	2.839	3.995	[77]	11.98	[77]

[48,49]. On the other hand, it is also known that Ce^{3+} shows strong $4f$-$5d$ absorption and $5d$-$4f$ luminescence from UV to visible range in the Ce^{3+}-doped compounds [24,49–51]. The wavelength variations in different host crystals are caused by the shift of the $5d$ energy levels. Fig. 4 shows the schematic energy diagram of Ce^{3+}:$5d$ energy levels. For the d orbital, the orbital angular momentum, l, is 2, so there are five possible states ($=2l+1$). If the spin-orbit coupling of Ce^{3+} ion in the free ion state is ignored, the $5d$ orbital states degenerate. Assuming Ce^{3+} ion in the spherical electrostatic field caused by anion coordination, the five states still degenerate, but the $5d$ energy can be shifted by the centroid shift which is defined as the lowering of the energy of the Ce^{3+} $5d$-configuration relative to the value for as a free ion (6.35 eV) [52]. The centroid shift is determined by the chemical (covalence) and physical (polarizability) properties of the anions coordinating Ce^{3+}. Occupying a center of a specific anions polyhedron site, Ce^{3+} ion is affected by the crystal field splitting which is mainly determined by the size and shape of the first anion coordination polyhedron around Ce^{3+}. For instance, the $5d$ energy level is split into t_{2g} (d_{xy}, d_{xz}, d_{yz}) and e_g (d_{x2-y2},d_{z2}) in the octahedral coordination. The splitting energy between t_{2g} and e_g orbitals in an octahedral field (Δ_O) can often be expressed as the crystal field splitting parameter ($10Dq$) [53]. Compared with the degenerated $5d$ level in the spherical field, the t_{2g} orbitals are stabilized by $-0.4 \times \Delta_O$ and the e_g orbitals are un-stabilized by $+0.6 \times \Delta_O$. On the contrary, in a cubic polyhedron, the t_{2g} orbitals are un-stabilized and the e_g orbitals are stabilized. Assuming the same bond length of Ce^{3+}-O^{2-} in the cubic polyhedron as that in the octahedral polyhedron, the splitting energy in the cubic field (Δ_C) becomes $8/9 \times \Delta_O$ [54]. Compared with the degenerate $5d$ level in the spherical field, the e_g orbitals are stabilized by $0.6 \times \Delta_C$ and the t_{2g} orbitals are un-stabilized by $0.4 \times \Delta_C$. Therefore, under the same condition of Ce^{3+}-O^{2-} bond length, the $5d$ energy of e_g orbital in the cubic symmetry becomes much lower than that of t_{2g} in octahedral symmetry theoretically. In the dodecahedral site in garnet structure, the configurations of the eight oxide ions around Ce^{3+} ion are displaced from the cubic polyhedron and then becomes a disordered square anti-prim (dodecahedron). In this case, the e_g and t_{2g} orbitals split more. The splitting between the lowest $5d_1$ and the second lowest $5d_2$ is noted as Δ_{12} and the normal crystal field splitting between the lowest $5d_1$ and the highest $5d_5$ is noted as ε_{cfs} [25]. As a result, a significant red shifting of the $4f$-$5d_1$ absorption can be observed in the garnet-type structure materials.

The $4f$-$5d_1$ absorption band exhibits a broad spectral shape as a

result of large configurational offset for $5d_1$ exited state and electron-phonon coupling as shown in Fig. 1. Unlike that the $4f$ orbital is inner orbital and shielded by filled $5s$ and $5p$ shells, the outer $5d$ orbital is not shielded. Thus, the equilibrium distance between $Ce^{3+}(4f$ ground state)-O^{2-} is different from that between $Ce^{3+}(5d$ excited state)-O^{2-}, which results in large configurational offset in the configurational co-ordinate diagram. Also, the excited $5d$ electron is strongly coupled with various lattice vibration modes (phonons) due to the non-shielded outer orbital. According to the Franck-Condon principle, the $4f$ electron can be excited into the $5d$ state coupling with some phonons directly. The degree of electron-phonon interaction is expressed by Huang-Rhys parameter (S). With increasing Hunag-Rhys parameter, the electron-phonon interaction becomes stronger. The Stokes shift energy has the following relationship, (Stokes shift energy) = $2S\hbar\omega$. Here, $\hbar\omega$ is phonon energy. For the specific garnet compounds which do not have inhomogeneous broadening, sometimes sharp zero-phonon line (ZPL) and phonon lines can be observed in absorption, PLE and PL spectra at low temperature. Also, the Hunag-Rhys parameter can be obtained using the relationship between ZPL intensity (I_{ZPL}) and total emission intensity (I_0), $I_{ZPL} = I_0 \times exp(-S)$ [21].

2. Variation of Ce^{3+}:5d-4f luminescence wavelength in garnet

The $5d$ energy splitting of Ce^{3+} in the garnet structure can be interpreted approximately as explained above. In this section, based on the experimental data of Ce^{3+}-doped garnets, we focus on the contributions of the centroid shift and the crystal filed to the red shifting of $5d_1$ energy. Dorenbos already collected the spectroscopic data of (Gd, Y, Lu)$_3$(Al$_{1-x}$Ga$_x$)$_5$O$_{12}$:Ce^{3+} and plotted the $5d_1$ and $5d_2$ energy as a function of red shifting parameter ($D(1, 3+,A)$), finding a clear trend between $D(1,3+,A)$ and Δ_{12} [25]. Here, the $D(1, 3+,A)$ is expressed by

$$D(1,3+,A) = E_{fd_{ave,free}} - E_{f5d1,A} - 0.23 \qquad (1)$$

where $E_{fd_{ave,free}}$ is the average energy of $4f$-$5d$ absorption in the free ion (6.35 eV), $E_{f5d1,A}$ is the lowest $4f$-$5d$ absorption energy (eV) in compound A, 0.23 eV is the difference between $E_{fd_{ave,free}}$ and the lowest $4f$-$5d$ ($^2D_{3/2}$) energy in the free ion as shown in Fig. 4. In order to confirm that the trend between the red shift and Δ_{12} observed in series of (Gd, Y, Lu)$_3$(Al$_{1-x}$Ga$_x$)$_5$O$_{12}$:Ce^{3+} can be applied for all the other Ce^{3+}-doped garnets listed in Table 1, the $5d_1$, $5d_2$ and e_g energies of extra garnet phosphors are plotted as a function of red shifting parameter, $D(1, 3+,A)$, as shown in Fig. 5. As proposed by Dorenbos, the Ce^{3+}-doped rare-earth aluminum gallium garnets represented by $(RE)_3$(Al,Ga)$_5$O$_{12}$ (RE = Gd, Y, Lu) garnets shows good proportionality between redshift and the Δ_{12} splitting where we added the data of Gd$_1$Y$_2$(Al, Ga)$_5$O$_{12}$, Gd$_2$Y$_1$(Al, Ga)$_5$O$_{12}$ and Y$_3$Sc$_2$(Al,Ga)$_3$O$_{12}$ garnets doped with Ce^{3+}. The fact that the large splitting of Δ_{12} follows the red-shifting of $4f$-$5d_1$ absorption implies that the changing redshift within the (Gd, Y, Lu)$_3$(Sc, Al, Ga)$_5$O$_{12}$ garnets is almost controlled by changing the crystal field splitting and that the change in the centroid shift have very minor contribution.

2.1. Relationship between centroid shift and composition

Fig. 5 also shows how the $5d_1$ and $5d_2$ energies in some garnets containing either Si or Ge (red hexagon, blue pentagon and green star) do not follow the trend of (Gd, Y, Lu)$_3$(Sc, Al, Ga)$_5$O$_{12}$ garnets. The large or small Δ_{12} does not show red-shifting or blue-shifting always, which implies that the centroid shift can be changed largely in the silicate and germanate garnets, such as (Sr,Ca)$_3$(Lu,Y,Sc)$_2$(Si,Ge)$_3$O$_{12}$, Lu$_2$Mg$_2$Al$_2$Si$_2$O$_{12}$, Lu$_2$Ca$_1$Mg$_2$Si$_3$O$_{12}$ and Mg$_3$Y$_2$(Si,Ge)$_3$O$_{12}$, compared with (Gd, Y, Lu)$_3$(Sc, Al, Ga)$_5$O$_{12}$ garnets. Thus, the centroid shift for the Ce^{3+}-doped garnet materials including (Gd, Y, Lu)$_3$(Sc, Al, Ga)$_5$O$_{12}$ garnets should be reconsidered. To check the centroid shift, it is necessary to observe all the $5d$ energy levels. However, in the Ce^{3+}-doped garnets, it is difficult to observe all the $5d$ energy levels because of the

overlapping between the band-to-band and the $4f$-$5d_{3,4,5}$ absorptions. So far, all the 5d energy levels of Ce^{3+} were determined only in two garnets of Lu$_3$Al$_5$O$_{12}$(LuAG) [25,78] and Y$_3$Al$_5$O$_{12}$(YAG) [25,79,80] by the experimental results. To increase the data of various garnet hosts, the photoluminescence excitation spectra of Ce^{3+}-doped LuAG, (Lu$_{0.5}$Y$_{0.5}$)$_3$Al$_5$O$_{12}$(LuYAG), YAG, Y$_3$Sc$_2$Al$_3$O$_{12}$ (YSAG) and Y$_3$Sc$_2$Ga$_3$O$_{12}$ (YSGG) that have relatively wide bandgap were measured as shown in Fig. 6a. In these series of garnets, in addition to the $5d_1$ and $5d_2$ bands at around 450 and 350 nm, respectively, other PLE bands were observed between 200 and 240 nm, which are considered as $5d_{3,4,5}$ bands. Only in YAG:Ce^{3+} and LuAG:Ce^{3+}, the zero-phonon line and phonon lines were observed in $4f$-$5d_1$ PLE band at around 450 nm because the [B] and (C) sites are substituted by only Al ions which leads to small inhomogeneity around Ce^{3+} ion. The ZPL intensity with respect to the $4f$-$5d_1$ PLE band in LuAG:Ce^{3+} is weaker than that in YAG:Ce^{3+}, which indicates that the Huang-Rhys parameter in LuAG:Ce^{3+} is larger than that in YAG:Ce^{3+}. This result shows good agreement with the reported Huang-Rhys parameters for YAG:Ce^{3+} (S = 6) [21] and LuAG:Ce^{3+} (S = 9) [81]. Focusing the transition wavelength, in the order of YAG, LuYAG and LuAG, the $5d_1$ is blue-shifted, the $5d_2$ is red-shifted and the set of $5d_{3,4,5}$ is blue-shifted. For the YSAG and YSGG, with increasing Ga content, the $5d_1$ is blue-shifted and the $5d_2$ is red-shifted as observed in (Lu,Y)AG garnet, but the set of $5d_{3,4,5}$ is red shifted. In 2015, we reported the PLE spectra of Ce^{3+}-doped Y$_3$Al$_4$Ga$_1$O$_{12}$ (YA4G1G), Y$_3$Al$_3$Ga$_2$O$_{12}$ (YA3G2G) and Y$_3$Al$_2$Ga$_3$O$_{12}$ (YA2G3G) in the VUV to UV range [41]. In this Y$_3$Al$_{5-x}$Ga$_x$O$_{12}$, with increasing Ga content, the $5d_1$ is blue-shifted, the $5d_2$ is red-shifted and the set of $5d_{3,4,5}$ is red shifted. Also, (Gd,Y)$_3$Al$_{5-x}$Ga$_x$O$_{12}$:Ce^{3+} shows the similar energy shifting of $5d$ levels for Ga content to that in the Y$_3$Al$_{5-x}$Ga$_x$O$_{12}$:Ce^{3+} [57]. These complicated shifting in different series of garnets can be caused by a balance of centroid shift (ε_c) and crystal filed splitting (Δ_C and Δ_{12}). To look in the details of $5d_{3,4,5}$ bands, the enlarged PLE spectra in the energy scale are shown in Fig. 6b. The PLE band at around 225 nm does not show a simple symmetric structure. It is known that the PLE band of Ce^{3+} at around 225 nm in the YAG and LuAG is also asymmetric [78,79]. This set of bands can be deconvoluted by Gaussian functions. As a fitting condition, three PLE bands related to $5d_{3,4,5}$ are assumed at around 225 nm with keeping bandwidths constant and one band is considered at about 260 nm that was reported as the defect absorption [80,82]. For the exciton absorption, an exponential baseline was considered. However, the fitting error was still significant because of some unknown absorption bands. Extra PLE bands were also assumed for the fitting. The resulting fitting curves reasonably match the spectra, the bandwidth of $5d_{3,4,5}$ are within 0.31–0.32 eV for (Lu,Y)$_3$Al$_5$O$_{12}$. This bandwidth is similar to those of the $5d_1$ and $5d_2$ bands. The $5d_{3,4,5}$ position in YAG and LuAG are in line with the previously assigned values in YAG by Tanner [80] and LuAG by Dorenbos [25]. For YSAG and YSGG, the $5d$ bandwidths are slightly broadened probably due to the inhomogeneous broadening.

From the obtained data of $5d_{1\sim5}$ excitation bands, the ε_c, ε_{cfs}, Δ_C and Δ_{12} are estimated and summarized as shown in Table 2. In addition, the Y$_3$Al$_{5-x}$Ga$_x$O$_{12}$:Ce^{3+} data re-analyzed by us in a previous paper [41] and the calculated Ca$_3$Sc$_2$Si$_3$O$_{12}$:Ce^{3+} data reported by Zhou [83] are also added in Table 1. By changing host materials, the ratio of ε_c and crystal filed splitting are changed. To visualize this change, the stacking column chart of different parameters that contribute to the red-shifting parameter is shown in Fig. 7. Here, the orange area shows the ε_c subtracted by 0.23eV, the blue area reflects the normal crystal field contribution in the cubic field (Δ_C) which was estimated from the subtraction of centroid energy for $5d_1$ and $5d_2$ ($E_{centro5d1,2}$) from the centroid energy for $5d_{1\sim5}$($E_{centro5d1\sim5}$) and the purple area reflects the contribution of the crystal filed splitting between $5d_1$ and $5d_2$, which was estimated by half of Δ_{12}. The centroid shift in LuAG, LuYAG and YAG is almost the same as each other as expected from the trend of Δ_{12} as a function of $D(1,3+,A)$ in Fig. 5 and as proposed by Dorenbos [25].

京都大学
KYOTO UNIVERSITY

J. Ueda and S. Tanabe

京都大学学術情報リポジトリ
KURENAI 紅
Kyoto University Research Information Repository

Optical Materials: X 1 (2019) 100018
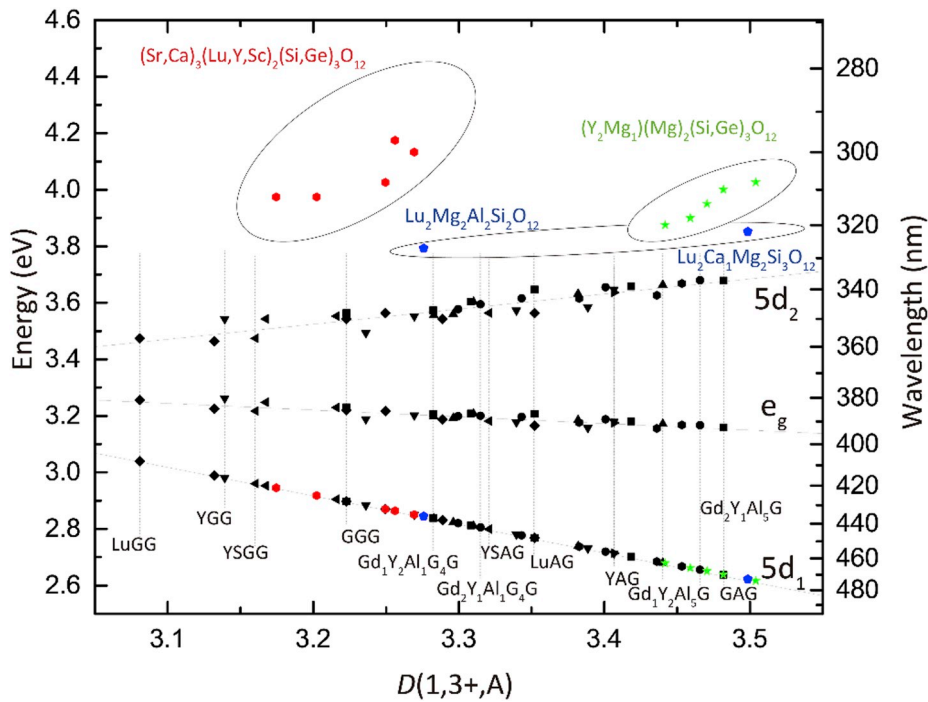
Fig. 5. Energy of excitation to the first two 5d-levels (5d_1, 5d_2) and centroid energy of 5d_1 and 5d_2 (e_g) of Ce^{3+} in garnet compounds against the red shift energy of D (1,3 + ,A). (For interpretation of the references to color in this figure legend, the reader is referred to the Web version of this article.)

Fig. 6. (a) PLE spectra of Ce^{3+} luminescence in LuAG, LuYAG, YAG, YSAG and YSGG from VUV to visible ranges. (b) Enlarged PLE spectra at around 5.5 eV in energy scale for deconvolution.

Table 2
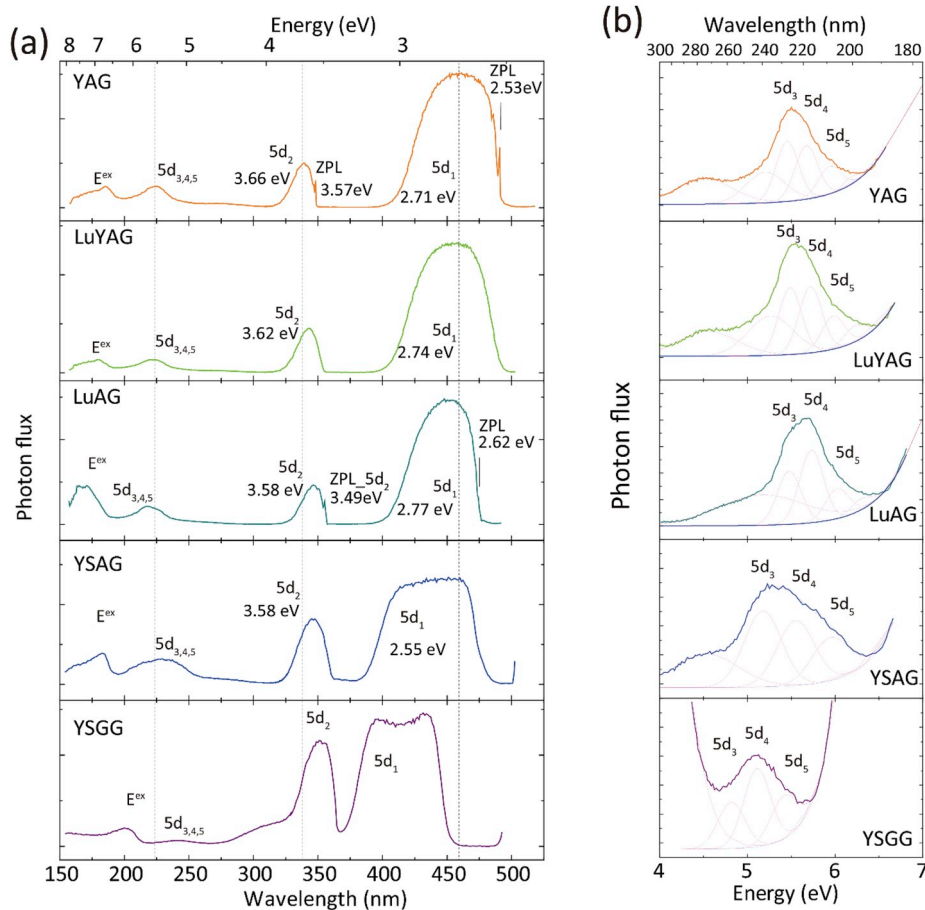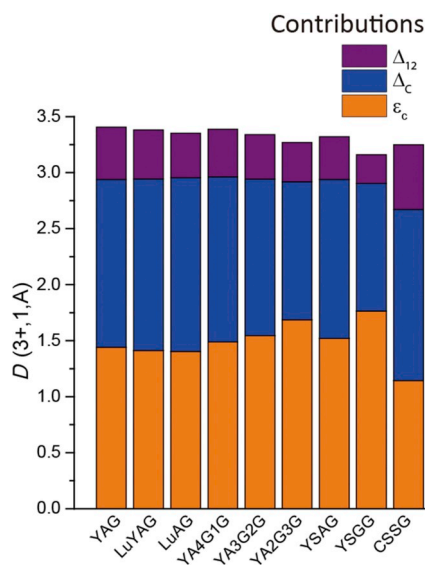Collected energetic parameters of $5d_1$, $5d_2$, $5d_3$, $5d_4$ and $5d_5$ and calculated parameters of ε_c, ε_{cfs}, Δ_c, Δ_{12} from the $5d_{1-5}$ energies in Ce^{3+}-doped garnet hosts.

Host	Ref.	$5d_1$	$5d_2$	$5d_3$	$5d_4$	$5d_5$	ε_c	ε_{cfs}	Δ_C	Δ_{12}
$Y_3Al_5O_{12}$ (YAG)	[25]	2.71eV	3.65eV	5.51eV	5.66eV	6.05eV	1.64eV	3.34eV	2.56eV	0.94eV
		457 nm	340 nm	225 nm	219 nm	205 nm				
	This work	2.71eV	3.66eV 339 nm	5.45 eV	5.66eV	5.94eV	1.63eV	3.23eV	2.50eV	0.95eV
		457 nm		228 nm	219 nm	209 nm				
$Lu_3Al_5O_{12}$ (LuAG)	[25]	2.77eV 448 nm	3.56eV	5.41eV 229 nm	5.64eV	6.02eV	1.67eV	3.25eV	2.53eV	0.79eV
			348 nm		220 nm	206 nm				
	This work	2.77eV 448 nm	3.58eV 346 nm	5.48 eV 226 nm	5.73 eV 216 nm	6.02 eV 206 nm	1.63eV	3.25eV	2.57eV	0.81eV
$Lu_{1.5}Y_{1.5}Al_5O_{12}$ (LuYAG)	This work	2.74eV	3.62eV	5.49eV	5.72eV	5.98eV	1.64eV	3.24eV	2.55eV	0.88eV
		453 nm	343 nm	226 nm	217 nm	207 nm				
$Y_3Al_4Ga_1O_{12}$ (YA4G1G)	[41]	2.73eV	3.58eV	5.29eV	5.6eV	5.94eV	1.72eV	3.21eV	2.46eV	0.85eV
		454 nm	346 nm	234 nm	221 nm	209 nm				
$Y_3Al_3Ga_2O_{12}$ (YA3G2G)	[41]	2.78eV	3.57eV	5.18eV	5.49eV	5.85eV	1.78eV	3.07eV	2.33eV	0.79eV
		446 nm	347 nm	239 mm	226 nm	212 nm				
$Y_3Al_2Ga_3O_{12}$ (YA2G3G)	[41]	2.85eV	3.55eV	(4.93eV)	(5.25eV)	(5.59eV)	1.92eV	2.74eV	2.06eV	0.70eV
		435 nm	349 nm	(252 nm)	(236 nm)	(222 nm)				
$Y_3Sc_2Al_3O_{12}$ (YSAG)	This work	2.86eV	3.56eV	5.17eV	5.55eV	5.95eV	1.73eV	3.09eV	2.35eV	0.70eV
		443 nm	348	240 nm	225 nm	208 nm				
$Y_3Sc_2Ga_3O_{12}$ (YSGG)	This work	2.96eV	3.47eV	(4.82eV)	(5.11eV)	(5.42eV)	1.99eV	2.46eV	1.9eV	0.51eV
		419 nm	357 nm	(257 nm)	(243 nm)	(229 nm)				
$Ca_3Sc_2Si_3O_{12}$ (CSSG)	[82]	2.87eV	4.02eV	5.59eV	6.1eV	6.31eV	1.37eV	3.44eV	2.56eV	1.15eV
		432 nm	308 nm	222 nm	203 nm	197 nm				

Fig. 7. Details of red shifting in host A. The contribution of centroid shift, crystal filed splitting by cubic filed (Δ_C) and crystal filed splitting of $5d_1$ and $5d_2$ (Δ_{12}) are estimated from ε_c-0.23 eV, $E_{centro5d1\sim5}$($5d_{1\sim5}$ centroid energy)-$E_{centro5d12}$($5d_{1,2}$ centroid energy) and $\Delta_{12}/2$, respectively. (For interpretation of the references to color in this figure legend, the reader is referred to the Web version of this article.)

However, the centroid shift of YAGG, YSAG and YSGG are much larger than that of LuAG, LuYAG and YAG despite the fact that YAGG, YSAG and YSGG follow the trend of Δ_{12} as a function of $D(1,3+,A)$ in Fig. 5. Also the centroid shift of CSSG is smaller than YAG. Thus, the centroid shift of Ce^{3+}:$5d$ orbitals is affected by the host composition.

It is known that the centroid shift depends not only on the atomic species of the anion but also on that of the cations that bind with the anions. Morrison proposed [84] that the centroid shift in fluoride compounds is caused by the correlated motion of the $5d$-electron and the electrons in the surrounding ligands. In the oxides and other compounds, the covalency also affects the centroid shift significantly. Thus, the centroid shift can be contributed by the correlated motion (ε_2) and covalency (ε_1), representing $\varepsilon_c = \varepsilon_1 + \varepsilon_2$. Subsequently, Dorenbos assumed the ε_1 is propotional to ε_2. Based on the Morrison's equation [84], Dorenbos introduced the effective polarizability [49] that is

named as spectroscopic polarizability (α_{sp}), and reported below equation,

$$\varepsilon_c = 1.79 \times 10^{13} \alpha_{sp} \sum_{i=1}^{N} \frac{1}{(R_i - 0.6\Delta R)^6} \tag{2}$$

where R_i is the distance from Ce^{3+} ion to the ligand i in pm, the centroid shift energy is in eV, α_{sp} is in Å^3 and $\Delta R = R_M - R_{Ce}$, R_M is the ionic radius of the cation that is replaced by Ce^{3+} with ionic radius R_{Ce} and $0.6\Delta R$ is the estimated amount of bond length relaxation. The spectroscopic polarizability can be expressed by $\alpha_{sp} = \alpha\left(1 + \frac{\varepsilon_1}{\varepsilon_2}\right)$ (α is the polarizability) and characterizes the chemical property of the anion ligand and the cations that bind with the anion ligands [85]. One may relate the average bond strength of the ligand electrons to the average electronegativity χ_{av} of the cations in the compound defined as

$$\chi_{av} = \frac{\sum_i n_i z_i \chi_i}{\sum_i n_i z_i} \tag{3}$$

where n_i is the number of cations of type i with charge $+z_i$ and electronegativity χ_i in the compound formula [85]. Dorenbos proposed also the following linear relationship [85],

$$\alpha_{sp} = \alpha_0(X) + \frac{b(X)}{\chi_{av}^2} \tag{4}$$

where $\alpha_0(X)$ is the limiting spectroscopic polarizability of anion X in the case of very large χ_{av}, i.e., in the case of strong binding of the anion valence electrons to cations. One may interpret $b(X)$ as the susceptibility of anion X to change its polarizability due to its bonding with coordinating cations. Dorenbos found that most of oxide compounds follow this linear relationship with 0.4 of $\alpha_0(O)$ and 4.6 of $b(O)$ parameters [52] as shown in the black line of Fig. 8. It is known that La^{3+}-based compounds, in which there are no bond-length-relaxation and no charge compensation for the Ce^{3+} ion, shows good agreement with this trend, while Ba^{2+}-based compounds, in which there are large bond-length-relaxation and charge compensation, are out of line [52]. In general, the data of Ce^{3+} in rare earth sites (La, Gd, Y, Lu) follows well Eq. (4), while some compounds such as Ce^{3+}-doped (RE)AlO_3 perovskites (RE = La, Gd, Y, Lu) show deviation [85]. However, Eq. (4) is still useful to discuss the trend of α_{sp} with respect to the host compositions as well as the average electronegativity. Fig. 8 shows the spectroscopic polarizability estimated from the obtained centroid shift energy and the crystal structure data in the Ce^{3+}-doped garnet as a function of χ_{av}^{-2}, and the general trend estimated using Eq. (4) with 0.4
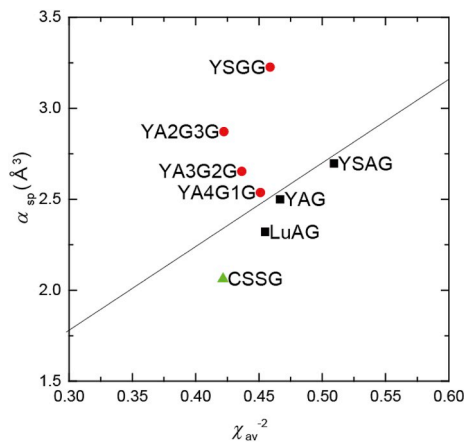
Fig. 8. The spectroscopic polarizability, α_{sp}, derived from the observed centroid against $\chi_{av}{}^{-2}$. The black line is estimated using Eq. (4) with 0.4 of $\alpha 0(O)$ and 4.6 of $b(O)$. Red dots represent Ga^{3+}-substituted barnets, black squares represent aluminate garnets, green triangle represents silicate garnet. (For interpretation of the references to color in this figure legend, the reader is referred to the Web version of this article.)

of $\alpha_0(O)$ and 4.6 of $b(O)$ parameters.

Aluminate garnets such as YAG, LuAG and YSAG and silicate garnet CSSG roughly follow the increase tendency in which α_{sp} increases with $\chi_{av}{}^{-2}$. This trend can be understood by the electronegativity difference of cations. Compared with the electronegativity of Al ($\chi_{Al} \sim 1.61$), that of Sc ($\chi_{Sc} \sim 1.36$) is much smaller. Consequently, YSAG has larger $\chi_{av}{}^{-2}$ and larger α_{sp} compared with YAG. For CSSG, the average electronegativity becomes larger ($\chi_{av}{}^{-2}$ becomes smaller) due to the significant large electronegativity of Si($\chi_{Sc} \sim 1.90$), so that α_{sp} is smaller compared with YAG. On the other hand, α_{sp} of gallium-substituted garnets does not follow this linear relationship. Since the electronegativity of Ga ($\chi_{Ga} \sim 1.81$) is larger than that of Al, α_{sp} of Ga-substituted garnets should be smaller than that of pure aluminate garnets. However, the observed α_{sp} in Ga-substituted garnets are totally opposite tendency, it increases with increasing Ga content in $Y_3Al_{5-x}Ga_xO_{12}$:Ce^{3+}. Dorenbos discussed that the compounds formed by the ions with the noble-gas electron configuration such as [Ne] electron configuration for Al^{3+} follow well the linear relationship in α_{sp} as a function of χ_{av}^{-2}, however, it has never been verified yet whether this tendency is followed also by Ga^{3+}-based compounds with filled 3d subshell, i.e., with non-noble-gas electron configuration [25]. Fig. 8 clearly shows that the garnet hosts formed by Ga^{3+} ions does not follow normal behavior observed in the garnet compounds formed by the ions with noble-gas electronic configuration. Therefore, α_{sp} of Ga-substituted garnet compounds is not predicted simply by electronegativity.

Dorenbos also investigated the correlation between α_{sp} and the optical basicity (Λ) [86]. The optical basicity is the electron donating power of oxygen ligands, and it was firstly estimated from the energy shifting of $^1S_0$–$^3P_1$ transition of Pb^{2+}, Bi^{3+} and Tl^+ [87–89]. The optical basicity can be calculated from the chemical composition as below [90],

$$\Lambda_{cal} = \frac{1}{2N_a} \sum_{i}^{N_c} \frac{z_i}{\gamma_i} \tag{5}$$

where N_a is the number of oxygen anions in the compounds formula. The summation is over all the N_c cations in the compounds formula, where z_i is the charge of cation i and γ_i is the optical basicity moderating parameter belonging to cation i. γ_i can be estimated from the Pauling electronegativity χ_i of the cation as below [90,91],

$$\gamma_i = 1.36(\chi_i - 0.25) \tag{6}$$

Dorenbos corrected the spectroscopic data of Ce^{3+} in some compounds
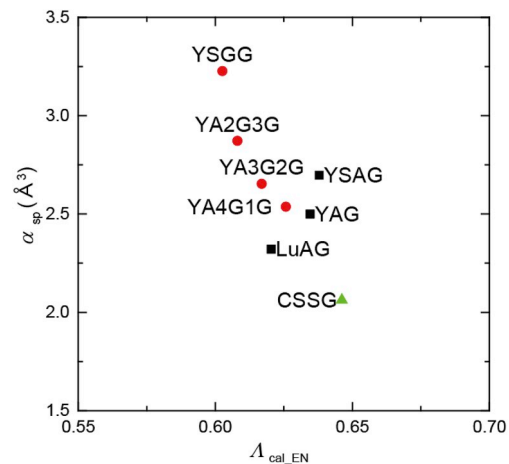
Fig. 9. The spectroscopic polarizability, α_{sp}, against the optical basicity estimated using parameter derived from electronegativity (Λ_{cal_EN}).

and estimated the optical basicity of host materials using Eqs. (5) and (6), and found a good linear relationship between Λ_{cal} and α_{sp} [86].

However, by plotting the α_{sp} as a function of the optical basicity estimated from the electronegativity using equations (5) and (6), the data of Ce^{3+}-doped garnet does not follow a general tendency in which the polarizability of oxygen ion becomes larger with increasing optical basicity as shown in Fig. 9 [86]. This is probably because of the method to calculate the optical basicity moderating parameter (γ) using Eq. (6), which was obtained from the linear fit of two values of γ_H in H_2O and γ_{Ca} in CaO against the electronegativity [90]. Eq. (6) is valid for some cations, but not for all the cations.

Thus, the optical basicity moderating parameter estimated from the experimental data (refractive index [92–94] or band gap energy [92,95]) may be better than that from the electronegativity. Fig. 10 shows the plot of α_{sp} with the obtained optical basicity (Λ_{cal_RI}) using the optical basicity moderating parameter estimated from the refractive index summarized by Duffy [96]. In this case, a clear linear relationship was observed. Empirically, we found that α_{sp} in the Ce^{3+}-doped garnets can be estimated from the following equation,

$$\alpha_{sp} = 10.34 \times \Lambda_{cal\_RI} - 5.36 \tag{7}$$

Therefore, in the Ce^{3+}-doped garnet, α_{sp} as well as centroid shift can be estimated from the optical basicity (Λ_{cal_RI}) which is calculated from the
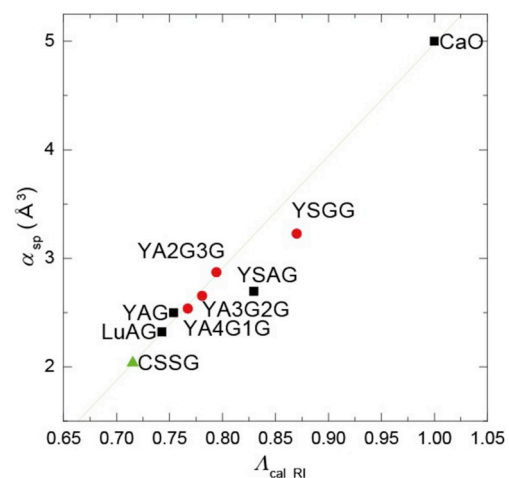
Fig. 10. The spectroscopic polarizability, α_{sp}, against the optical basicity estimate using the parameter derived from refractive index (Λ_{cal_RI}). The green line is a linear fitting curve. (For interpretation of the references to color in this figure legend, the reader is referred to the Web version of this article.)

optical basicity moderating parameter and the chemical composition.

2.2. Relationship between crystal field splitting and crystal structure

It is known that the crystal field splitting of Ce^{3+} in the garnet compounds is incredibly large. This is probably because of the local structure around Ce^{3+} ion. As mentioned in Fig. 5, the dodecahedral site has a disordered square anti-prism structure, whose distorted structure may induce extra crystal filed splitting of Δ_{12}. In general, the crystal field splitting ε_{cfs} becomes larger with decreasing the cation site size. Dorenbos reported the general tendency between ε_{cfs} and the average bond length modified by the lattice relaxation (R_{av}) from the spectroscopic and structural data of some Ce^{3+}-doped compounds [24,50,51,52]. The R_{av} is defined as

$$R_{av} = \frac{1}{N} \sum_{i=1}^{N} (R_i - 0.6\Delta R) \tag{8}$$

where R_i are the individual bond lengths to the N coordinating anions in the unrelaxed lattice [52]. $\Delta R = R_M - R_{Ln}$ with R_M the ionic radius of the cation that is replaced by the lanthanide Ln with ionic radius R_{Ln}, and $0.6\Delta R$ is the estimated amount of bond length relaxation. In the octahedral(octa), cubic, dodecahedal(dodeca) and cuboctahedral(cubo) coordination, crystal field splitting appeared to behave the following relationship,

$$\varepsilon_{cfs} = \beta_{poly}^Q R_{av}^{-2} \tag{9}$$

where β_{poly}^Q is a constant that depends on the type of coordination polyhedron and whether the lanthanide is trivalent (Q = 3+) or divalent (Q = 2+) [24,50,51,97]. Dorenbos estimated $\beta_{octa}^{3+} = 1.68 \times 10^5$ eV·pm^2 and $\beta_{octa}^Q : \beta_{cubic}^Q : \beta_{dodeca}^Q : \beta_{cubo}^Q = 1: 0.89: 0.79: 0.44$ for Ce^{3+} ion [24,50,51, 52, 97]. Here, the β_{dodeca}^Q value is based on the different dodecahedral with D_{2d}, C_1 or C_2 symmetry to that in garnet (β_{garnet}^Q) with D_2 symmetry [51]. Fig. 11 shows the crystal field splitting of ε_{cfs} dependence as a function of R_{av}. The observed tendency in the garnet phosphors is totally different from the reported trend of Ce^{3+} in all the polyhedron such as octahedaral, cubic and dodecahedral sites obtained using Eq. (9) as showing Fig. 11. As a result, the garnet group can be classified to the strongest crystal field splitting group. These results implies that general value of β_{garnet}^Q does not exist and it is probably variable because of the strong distortion.

Here, it should be noted that there are only fewer garnet hosts in which all the $5d_{1\sim5}$ bands can be observed as discussed in centroid shift, so that ε_{cfs} is not a comprehensive parameter for the discussion of

Fig. 12. ε_{cfs} of Ce^{3+}:5d against Δ_{12} in some Ce^{3+}-doped garnets in which all $5d_{1-5}$ were determined.

various series of garnet hosts. On the other hand, the $5d_1$ and $5d_2$ energy levels can be always observed, so that Δ_{12} can be a useful parameter. Fig. 12 shows the ε_{cfs} dependence as a function of Δ_{12}. A good correlation was found, so instead of ε_{cfs}, Δ_{12} can be used as a parameter for the discussion of crystal filed splitting. By fitting using linear function except the point of $Ca_3Sc_2Si_3O_{12}$:Ce^{3+}, the below function was obtained,

$$\varepsilon_{cfs} = 2.08\Delta_{12} + 1.42 \text{ in eV unit} \tag{10}$$

Fig. 13 shows Δ_{12} as a function of lattice constant using collected data as shown in Table 1. In each specific series of garnets such as GAGG ($Gd_3Al_{5-x}Ga_xO_{12}$), G2YAGG ($Gd_2Y_1Al_{5-x}Ga_xO_{12}$), G1Y2AGG ($Gd_1Y_2Al_{5-x}Ga_xO_{12}$), YAGG ($Y_3Al_{5-x}Ga_xO_{12}$), LuAGG ($Lu_3Al_{5-x}Ga_xO_{12}$), YSAGG ($Y_3Sc_2Al_{3-x}Ga_xO_{12}$) and MYSGG ($Mg_3Y_2Si_{3-x}Ge_xO_{12}$), Δ_{12} increases with decreasing the lattice constant, while in all garnet compositions no tendency was observed. Even though the Δ_{12} are plotted by average bond length modified by lattice relaxation, there is no tendency as shown in Fig. 14.

It is obvious that we should take into account the distortion of the dodecahedral site in the garnet hosts. Thus, we collected the crystal structure data of garnet compounds based on the ICSD(Inorganic Crystal Structure Database) and summarized the bond length related to
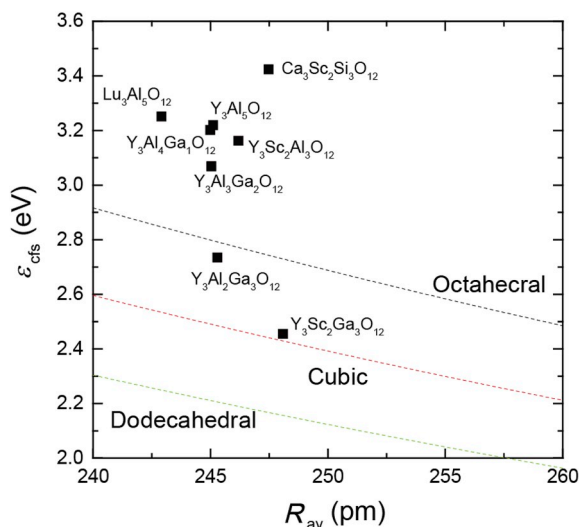

Fig. 11. Crystal field splitting, ε_{cfs}, of Ce^{3+} against R_{av}. The dashed lines are obtained from Eq. (9) with β_{poly}^Q parameters.
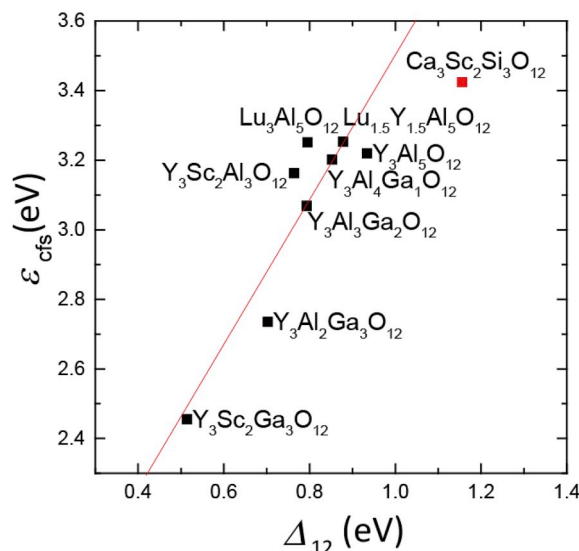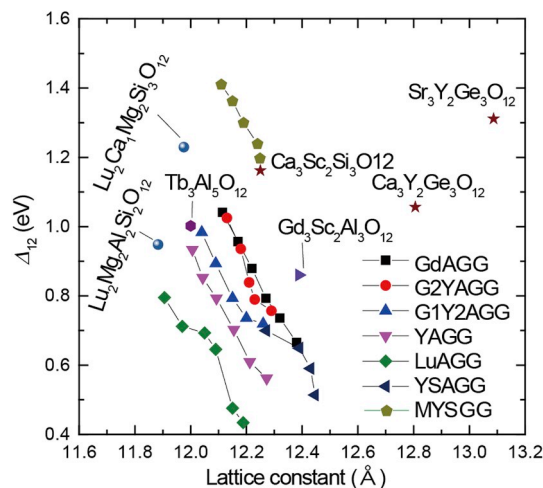

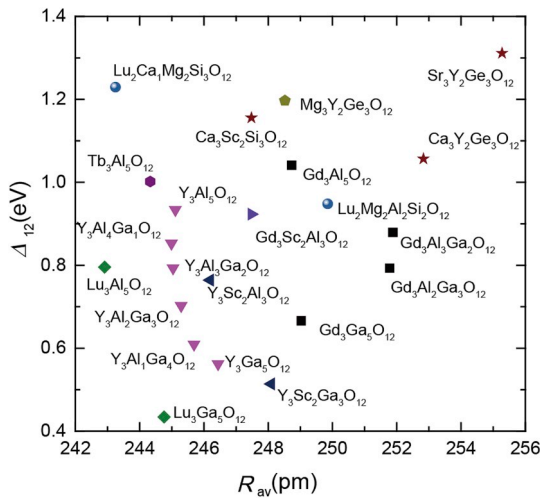**Fig. 13.** Δ_{12} against lattice constant in various Ce^{3+}-doped garnets.

Fig. 14. Δ_{12} against R_{av} in Ce^{3+}-doped garnets in which the crystal structure data was reported.

Fig. 16. Δ_{12} against $d_{83}/(d_{48} \cdot R_{av})$ of various Ce^{3+}-doped garnets. The red line is a fitting result. For $Mg_3Y_2Ge_3O_{12}$ and $Ca_3Sc_2Si_3O_{12}$, two different data from the different group were plotted. (For interpretation of the references to color in this figure legend, the reader is referred to the Web version of this article.)

the dodecahedral {A} site as shown in Table 1. Wu et al. showed a tendency between the luminescence wavelength and the disorder factor defined as the ratio of edge lengths of dodecahedral, d_{88}/d_{81} [34]. As shown in Fig. 3b, d_{88} is the edge shared by another dodecahedral, d_{81} is one of the non-sharing edges. However, d_{88}/d_{81} is not a perfect parameter to explain the crystal field splitting as shown in Fig. 15a. Recently, Song et al. reported the trend between the distortion and the radio of d_{88}/d_{48} [35]. The d_{84} is the edge shared by another tetrahedral site as shown in Fig. 3b. Fig. 15b shows the Δ_{12} versus d_{88}/d_{48} plot, where a relatively better linearity compared with the plot versus d_{88}/d_{81} was observed. Here, we found that the ratio of d_{83}/d_{48} is a much better parameter to predict Δ_{12} as attested by the good linearity in Fig. 15c. The d_{83} is the non-sharing edge of the dodecahedral site which is the approximate diagonal of the square formed by two d_{88} and two d_{86} edges (Fig. 3b). The ratio d_{83}/d_{48} is the parameter to describe the distortion of the dodecahedral site, but it does not fully consider the contribution of the size of the dodecahedral site. In order to include this contribution, we propose a new parameter dividing d_{83}/d_{48} by the R_{av}. Fig. 16 shows the good linearity for the Δ_{12} dependence of d_{83}/d_{48} divided by R_{av}. However, some points such as green pentagon ($Mg_3Y_2Ge_3O_{12}$), purple hexagon ($Tb_3Al_5O_{12}$), dark blue left triangle ($Y_3Sc_2Al_3O_{12}$) and wine red star ($Ca_3Sc_2Si_3O_{12}$) do not perfectly follow the trend. Based on the linear fit done without considering the above four points, we found the Δ_{12} can be estimated empirically by the crystal structure data of garnet as,
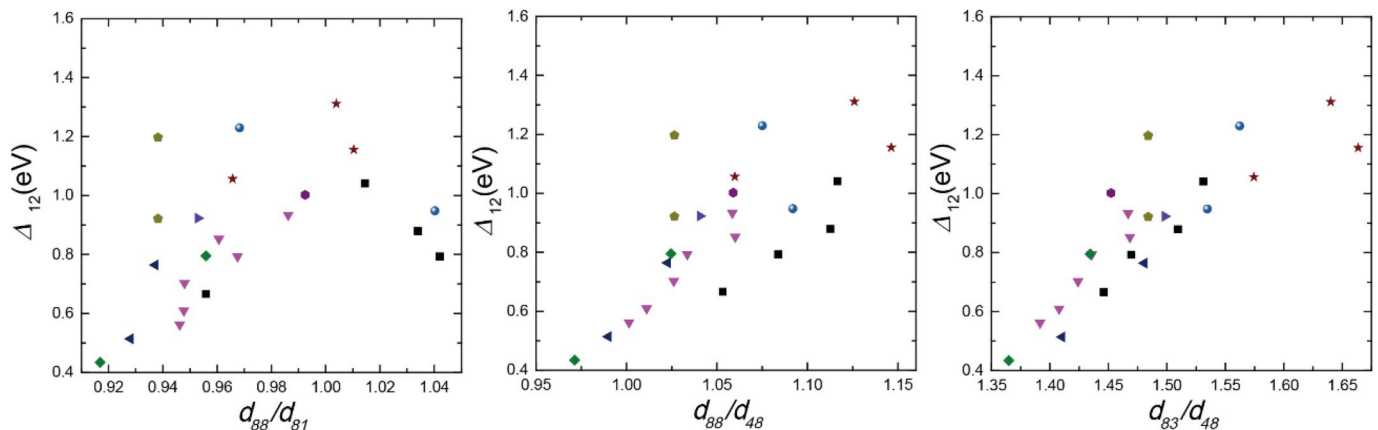
$$\Delta_{12} = 942 \times \frac{d_{83}}{d_{48}} \frac{1}{R_{av}} - 4.78 \tag{11}$$

Here, Δ_{12} is in eV unit and R_{av} is in pm unit.

For the $Mg_3Y_2Ge_3O_{12}$ host, we reported the significant inhomogeneity around Ce^{3+} ion which causes a substantial mismatch between the absorption spectrum and photoluminescence excitation spectrum. If we calculate the Δ_{12} from the absorption spectrum of $Mg_3Y_2Ge_3O_{12}$ [75], the point follows the line as shown in Fig. 16. In addition, for $Ca_3Sc_2Si_3O_{12,}$ Sharma et al. reported different $5d_1$ and $5d_2$ excitation band at 440 and 287 nm [23] from that at around 440 and 310 nm in other reports [83,98]. If we take Sharma's data, Δ_{12} also becomes closer to the fitting line. Therefore, the obtained function may be used as a useful tool to confirm the $5d_1$ and $5d_2$ assignment and the energy position.

3. Luminescence quenching of Ce^{3+} in garnets

For the optical devices based on the $5d$-$4f$ luminescence of Ce^{3+}, the (thermal) quenching of the luminescence becomes a big issue. Until the ~1990s, the luminescence quenching of the $5d$-$4f$ transition was often explained by the thermally activated crossover mechanism by using the configuration coordinate (CC) diagram [37,99]. The thermally activated crossover process, as shown by the red arrow in the CC diagram of Fig. 1 is the nonradiative relaxation process from the excited $5d$

Fig. 15. Δ_{12} against (a) d_{88}/d_{81}, (b)d_{88}/d_{48} and (c)d_{83}/d_{48}. The symbols are the same as that in Fig. 14.
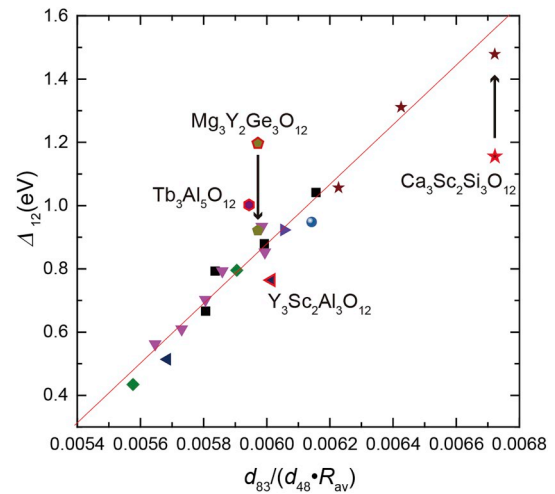
potential curve to the lower 4*f* potential curve through the crossing point. At the crossing point, the energy of 5*d* state coupling with a few phonons matches that of a higher 4*f* vibronic state and the resonant transition to the 4*f* state is followed by rapid non-radiative relaxation to the lower vibronic 4*f* states. The high 4*f* vibrational levels involved have their amplitude concentrated almost exclusively at the extremes of the parabola. Because of this, the thermally activated cross-over is often depicted as a thermally activated process with the energy difference between the lowest vibrational level of the excited state and the crossing point of the parabola as activation energy. The simple activation energy of crossover quenching in the CC diagram can be estimated by the zero-phonon energy, Huang-Rhys parameter and phonon energy if the anharmonicity of the potential curves and the temperature dependence of effective phonon energy are ignored [37]. This activation barrier decreases for a smaller energy difference between the states and a larger configurational off-set (large Huang-Rhys parameter and large phonon energy) [100].

For instance, the energy difference between the 5d_1 state and the next lower 4*f* ($^2F_{7/2}$) state for Ce^{3+}-doped YAG is significantly large (~ 3.1 eV), while for Pr^{3+}-doped YAG the energy difference between 5d_1 state and the next lower 4*f*($^3P_2$) state is much smaller (~ 1.5 eV) [100]. The YAG:Ce^{3+} and YAG:Pr^{3+} have almost the same Huang-Rhys parameter and phonon energy, so that the energy difference between the states determines the thermally activated quenching properties. Although the YAG:Pr^{3+} is likely to show the thermally activated crossover quenching, the Ce^{3+}-YAG is not likely to show it even at high temperatures due to the quite large energy difference. Also, the quenching temperature of 5*d*-4*f* luminescence in $Y_3Al_{5-x}Ga_xO_{12}$:Pr^{3+} increases with increasing Ga content up to x = 3 because the 5*d* energy shifts to higher. This result follows the trend of the thermally activated crossover quenching [100]. However, as explained in the introduction, the series of Ce^{3+}-doped garnets, such as $Y_3Al_{5-x}Ga_xO_{12}$, does not follow the tendency of the thermally activated cross-over quenching estimated from the configurational coordinate diagram; the ionization process should be considered.

Raukas, Happek and Yen et al. firstly demonstrated the existence of auto-ionization and thermally activated ionization (thermal ionization) quenching from the first 5d_1 excited level in Ce^{3+}-doped phosphors by photoconductivity analysis in the 1990s [101–103]. Auto-ionization is the electron transfer process without thermal assistance from the 5*d* excited state to the conduction band (CB) as shown in the dark green arrow of Fig. 17, while thermal ionization is the thermally activated electron transfer process as shown by the red arrow of Fig. 17. The combination of the photon excitation from the 4*f* ground state to the 5*d*

state and the auto-ionization from 5*d* to the CB is defined as photo-ionization while when the thermal energy supports the ionization process, we refer to the thermally assisted photoionization. The state in which the electron is located in the CB and the hole is trapped by the luminescent center is not stable, so that the recombination process occurs non-radiatively (quenching). Note that not all the ionized electrons recombine with the photo-oxidized luminescent center non-radiatively. Some of the ionized electrons can transfer back to the 5*d* excited state immediately or after trapping to intrinsic defects and de-trapping processes (persistent luminescence and delayed recombination luminescence) [10,11,104,105]. In any case, the thermally activated photo-ionization process leads to reduced light output. The quenching temperature, which is defined as the temperature at which the PL intensity or the lifetime becomes half of those at low temperature, is determined by the energy difference between the emitting excited state and the conduction band edge.

The thermal quenching of Ce^{3+} luminescence in garnets was already studied in 1973, when Weber measured the temperature dependence of the 5*d*-4*f* luminescence in YAG:Ce^{3+} and YAG:Pr^{3+} and reported that the lifetime of the 5d_1 excited state rapidly decreases above 600 K in YAG:Ce^{3+} [106]. He tried to explain the quenching process by non-radiative multiphonon relaxation from the 5*d* state to the 4*f* ground state. From the late 1970s, in order to understand the inability to obtain lasing of YAG:Ce^{3+}, the excited state absorption (ESA) from the lowest 5d_1 energy level was studied by some groups [107–109]. Pedrini et al. investigated the threshold energy of photoionization of Ce^{3+} in the YAG host by photoconductivity measurement and also suggested that the strong ESA is caused by the transition from 5d_1 to CB [109]. However, the 5d_1 excitation band was not observed in the photocurrent excitation spectrum [109]. In 1991, based on the rough agreement between the quenching activation energy (6500 cm^{-1}, 0.81 eV) estimated from the temperature dependence of lifetime and the 5d_1-CB energy gap estimated from the ESA peak (10000 cm^{-1}, 1.24 eV), Lyu and Hamilton suggested that the quenching process of YAG:Ce^{3+} is caused by the thermal ionization [110,111]. However, there had not been any direct evidence of the thermal ionization quenching process from the first 5d_1 excited level in any Ce^{3+}-doped garnets as well as YAG:Ce^{3+} until our report [112]; the excitation band corresponding to the 5d_1 energy level of Ce^{3+}-doped garnets had never been reported in the photocurrent excitation spectra although the 5d_2 band have been observed in $Gd_3Sc_2Al_3O_{12}$:Ce^{3+} by Happek et al. [113].

Since the thermal ionization quenching depends on the energy gap between the 5d_1 excited level and the bottom of the conduction band (Fig. 17), the CB engineering strategy can be adapted to investigate the
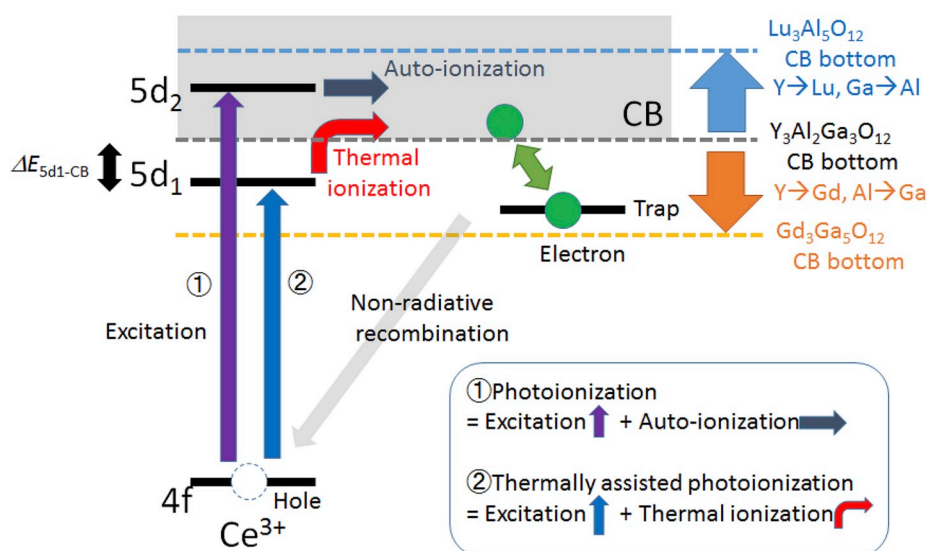

Fig. 17. Schematic diagram of ionization quenching process based on Ce^{3+}-doped $Y_3Al_2Ga_3O_{12}$ and the CB engineering for controlling the thermal ionization quenching process: With increasing Al or Lu content instead of Ga or Y, respectively, the CB bottom increases, while with increasing Ga or Gd content instead of Al or Y, respectively, the CB bottom decreases.

thermal ionization quenching. So far, the CB engineering strategy in Ce^{3+}-doped garnets have been used in the scintillator area to prevent the trapping of electrons by shallow traps [18,114], in the persistent phosphor area to control the persistent luminescence performance [11,115] and also in the phosphor area to understand the quenching process [55,60,112]. For instance, by considering the $Y_3Al_2Ga_3O_{12}$ host (Fig. 17), the CB bottom increases by substituting Y and Ga with smaller ions such as Lu and Al, respectively, while the CB bottom decreases by substituting Y and Al with larger ions of Gd and Ga, respectively. Therefore, the series of rare earth aluminum gallium garnets, such as $(Gd,Y)_3Al_{5-x}Ga_xO_{12}$ and $Y_3Sc_2Al_{3-x}Ga_xO_{12}$, became a key model compound to systematically investigate the quenching process. In this view, their optical and optoelectronic properties will be shown in chapter 3.1 and 3.2.

Note that in this review we focus on intrinsic quenching processes which should be observed in the ideal phosphor with dilute Ce^{3+} concentration. Extrinsic quenching processes, such as the concentration quenching and the energy transfer to some defects or impurity ions due to synthesis condition are not considered. The extrinsic quenching processes cause the deviation of quenching temperature or quantum yield [21,116]. For instance, Bachmann et al. reported the Ce^{3+} concentration dependence for the quenching temperature in the YAG host [21] and Lin et al. reported the down shifting of phonon frequency in YAG:Ce^{3+} with increasing Ce^{3+} concentration and suggested the correlation with the nonradiative process [116].

3.1. Quantum yield and thermal quenching

Quantum yield (QY) is defined as the ratio of emitted photons to absorbed photons. Fig. 18 shows the QY of Ce^{3+}:5d-4f luminescence in the $Gd_yY_{3-y}Al_{5-x}Ga_xO_{12}$:$Ce^{3+}$ (x = 0–5, y = 0–3) (GYAGG series) and $Y_3Sc_2Al_{3-x}Ga_xO_{12}$:$Ce^{3+}$ (x = 0–3) (YSAGG series) hosts [57,60], which were directly evaluated with an integrating sphere using blue light excitation (440 m–450 nm) and a spectrophotometer. The QY keeps almost constant or slightly decreases up to x~3 in all of the GYAGG garnet series with y = 0,1,2 and 3, while above x~3 the QY drops significantly. Also for the YSAGG series, the QY diminishes with increasing Ga content.

Fig. 19 shows the temperature dependence of Ce^{3+} luminescence in the $Y_3Al_{5-x}Ga_xO_{12}$ (YAGG series) and $Y_3Sc_2Al_{3-x}Ga_xO_{12}$ garnet hosts
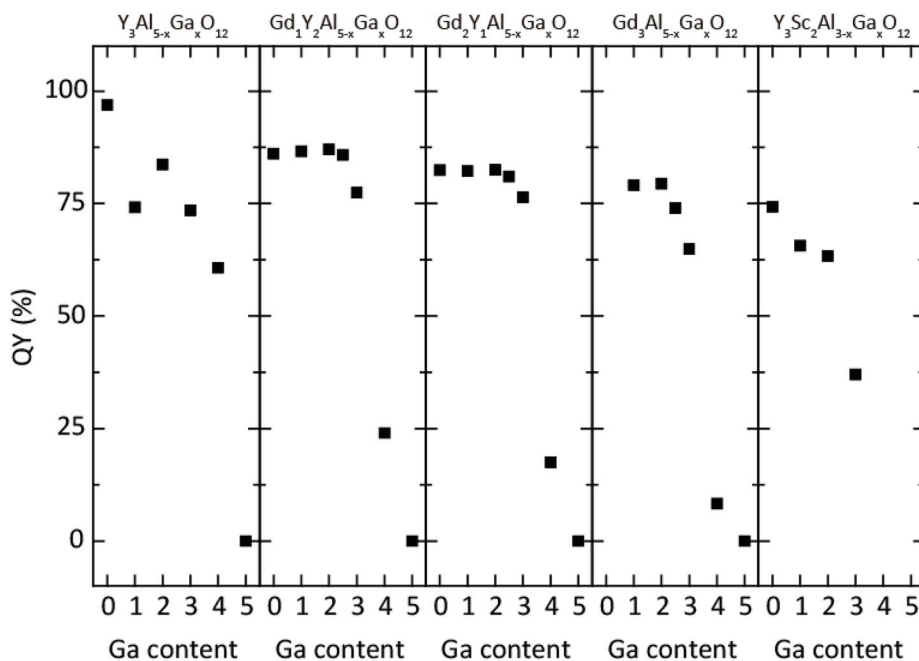

Fig. 19. Temperature dependence of integrated Ce^{3+}:5d-4f photoluminescence intensity excited by blue light in $Y_3Al_{5-x}Ga_xO_{12}$:Ce^{3+} [41] (Reproduced from Ref. [41] with permission from the Royal Society of Chemistry). and $Y_3Sc_2Al_{3-x}Ga_xO_{12}$:$Ce^{3+}$ [60] with different Ga content (Reproduced with permission from Ref. [60], copyright 2013, Elsevier). (For interpretation of the references to color in this figure legend, the reader is referred to the Web version of this article.)

[41,60]. All of the samples show that the PL intensity drops with increasing temperature. As expected from the QY results, the quenching temperature decreases with increasing Ga content in all the series of garnets. According to the single barrier model, the temperature dependence of the photoluminescence(PL) intensity can be expressed by below function,

$$I_{PL}(T) \propto \eta(T) = \frac{\Gamma_\nu}{\Gamma_\nu + \Gamma_0 \exp\left(-\frac{\Delta E}{kT}\right)} = \tau_f(T) \times \Gamma_\nu \tag{12}$$

where I_{PL} is the luminescence intensity, η is the quantum efficiency, Γ_ν is the radiative rate, Γ_0 is the attempt rate of the nonradiative process, ΔE is the activation energy, k is the Boltzmann constant, T is the temperature, τ_f is the fuluorescence lifetime.

Fig. 18. Quantum yield of Ce^{3+}: 5d-4f luminescence in five different garnet series with different Ga content excited by blue light (440 nm–450 nm) [57,60]. (Reproduced with permission from Refs. [57,60], copyright 2013&2018, Elsevier). The QY of $Y_3Al_{5-x}Ga_xO_{12}$:Ce^{3+} is private new data. (For interpretation of the references to color in this figure legend, the reader is referred to the Web version of this article.)
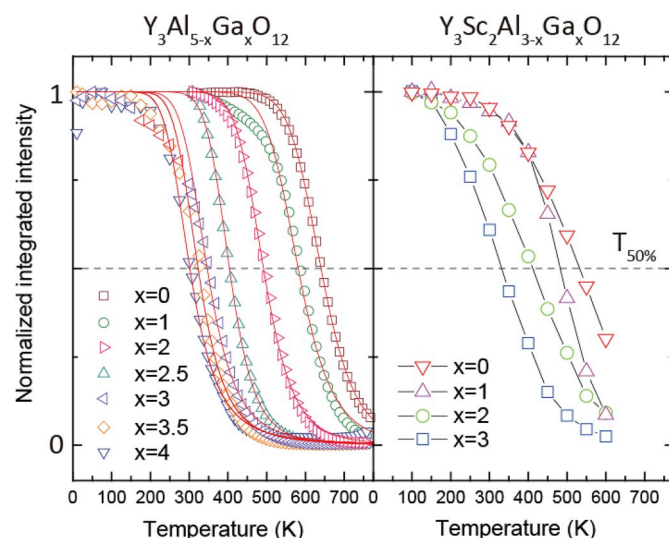
Using the definition of $T_{50\%}$ one obtains

$$T_{50\%} = \frac{\Delta E}{k \times ln\left(\frac{\Gamma_0}{\Gamma_v}\right)} \tag{13}$$

Clearly, with increasing Ga content in the series of YAGG and YSAGG hosts, the activation energy for the quenching process becomes smaller. These results observed in the QY and the temperature dependence of the PL intensity measurements contradict the tendency of the thermally activated crossover quenching. As shown in the previous chapters, the $5d_1$ energy increases with increasing Ga content instead of Al in the GYAGG and YSAGG series, which indicates that the activation energy of thermally activated crossover becomes larger. However, the experimental results show that the activation energy decreases with increasing Ga content. Therefore, it is supposed that the quenching process of these garnet hosts can be caused by the thermal ionization, but not by the thermally activated crossover.

3.2. Thermal ionization: photoconductivity measurements

In order to demonstrate the auto-ionization and the thermal ionization quenching from the $5d$ excited level in the Ce^{3+}-doped garnets, we have measured the photocurrent excitation (PCE) spectrum, which is a plot of photocurrent as a function of excitation wavelength [60,112]. Fig. 20 shows the schematic diagram of the PCE spectrum measurement system. In this system, an opaque garnet ceramic pellet was used, so that gold electrodes were deposited on the same side of the sample pellet which was partially masked by a tape of 1-mm width to separate the electrodes. The sample connected with two copper wires was mounted into a cryostat to control the sample temperature between 20 K and 300 K (Iwatani industrial gases Co., Ministat) or between 80K and 800 K (Advanced Research Systems, Helitran LT3). In addition, a sample chamber was always kept in a vacuum to suppress the surface current of the sample. The sample was excited by a combination of a 300-W Xe lamp (Asahi Spectra Co., Ltd, MAX-302) and a monochromator (Nikon, G250). A direct voltage of 300 V was applied to the sample, and photocurrents were measured with a digital electrometer (ADVANTEST, 8240).

To investigate the quenching process of Ce^{3+} luminescence in the series of $Y_3Al_{5-x}Ga_xO_{12}$ hosts, the PCE spectra of $Y_3Al_5O_{12}$(YAG), $Y_3Al_2Ga_3O_{12}$(YAGG) and $Y_3Ga_5O_{12}$(YGG) were examined (Fig. 21) [112]. At ambient temperature, no photocurrent was observed in the YAG:Ce^{3+} sample by excitation in the wavelength range from 300 to
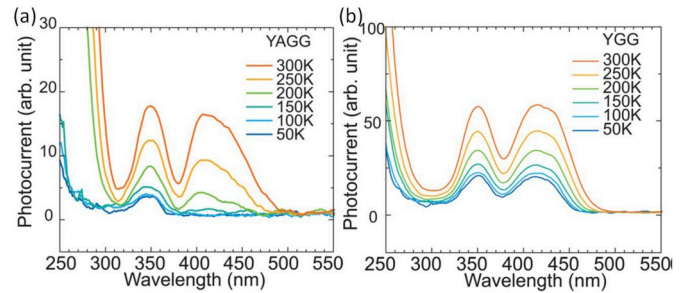

Fig. 21. Temperature variations of photocurrent excitation spectra of Ce^{3+} doped $Y_3Al_2Ga_3O_{12}$ (YAGG) and $Y_3Ga_5O_{12}$ (YGG) [112] (Reproduced with permission from Ref. [112], copyright 2011, American Institute of Physics).

550 nm. On the other hand, intense photocurrent excitation bands were observed at around 420 and 350 nm in the YGG:Ce^{3+} and the YAGG:Ce^{3+} samples at 300 K as shown in Fig. 21. Because peak wavelengths of these two bands correspond to the results in the absorption spectra of the YAGG:Ce^{3+} and YGG:Ce^{3+} samples, the PCE bands at around 420 and 350 nm are identified as the $4f$–$5d_1$ and $4f$–$5d_2$ transitions, respectively. These results of the PCE spectra show that the excited electrons at $5d_1$ and $5d_2$ levels transfer to the CB. Therefore, the quenching process of Ce^{3+} in the YAGG and YGG hosts can be caused by the ionization process. Fig. 22 shows the temperature dependence of the Ce^{3+}:$5d_1$-$4f$ photoluminescence intensity and the photocurrent intensity in the YAGG host [115]. With increasing temperature, the photoluminescence intensity decreases while the photocurrent increases monotonically. This inverse correlation demonstrates that the quenching process of Ce^{3+} in $Y_3Al_2Ga_3O_{12}$ is caused by thermal ionization.

Also, based on the temperature dependence of the PCE spectra, the energy level location can be discussed. In the PCE spectra at 50K, the photocurrent was observed only by the $5d_2$ excitation, but not by the $5d_1$ excitation in the YAGG:Ce^{3+} sample. In the YGG:Ce^{3+} sample, a significant photocurrent was observed by both $5d_1$ and $5d_2$ excitations even at low temperature. These phenomena can be understood by the relative position between the $5d$ levels and the CB. The $5d_1$ level in the YAGG:Ce^{3+} can be located just below the bottom of the CB, so that the photoconductivity from the $5d_1$ level to the CB can be induced by a thermally stimulated process. The fact that the PCE band of the $5d_2$ level in the YAGG:Ce^{3+} was observed at low temperature shows that the $5d_2$ level is located within the CB. On the other hand, in the YGG:Ce,
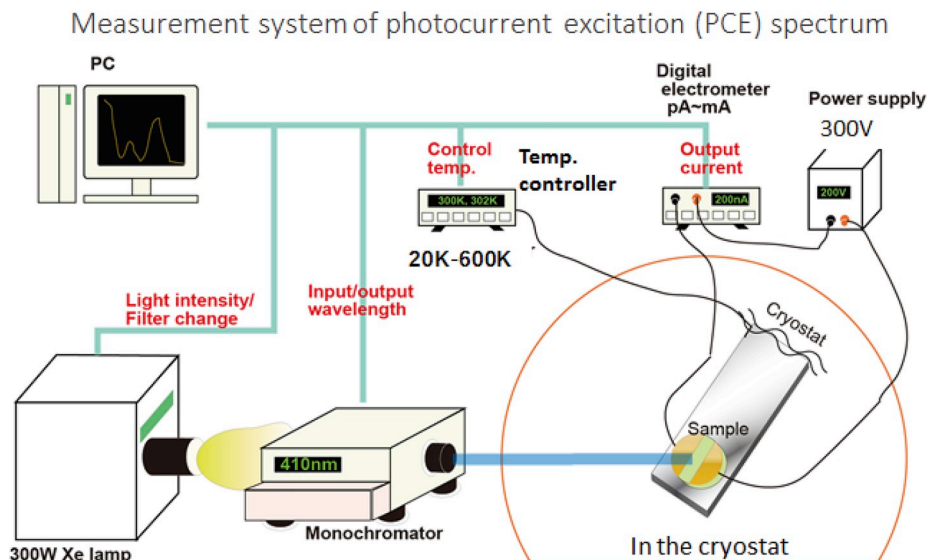

Fig. 20. Schematic diagram of photocurrent excitation spectrum measurement system.
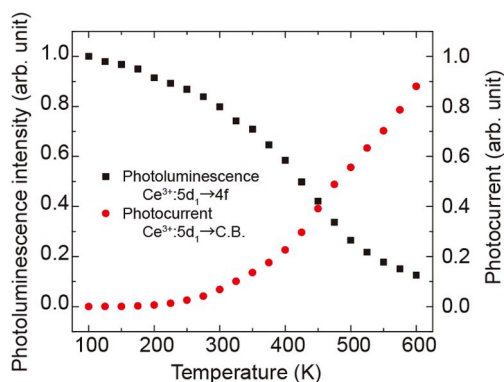
Fig. 22. Temperature dependence of photoluminescence and photocurrent in $Y_3Al_2Ga_3O_{12}:Ce^{3+}$ [115] (Reproduced with permission from Ref. [115], copyright 2015, the Ceramic Society of Japan).

the $5d_1$ and $5d_2$ level can be located within the CB, so that the quenching occurs by the autoionization.

The similar PCE spectra were also observed in another series of garnets. For the series of $Y_3Sc_2Al_{3-x}Ga_xO_{12}$ hosts as shown in Fig. 23a, the $Y_3Sc_2Ga_3O_{12}:Ce^{3+}$ sample shows strong $5d_1$ and $5d_2$ photocurrent excitation bands between 100 and 500 K while the $Y_3Sc_2Al_3O_{12}:Ce^{3+}$ sample does not show $5d_1$ and $5d_2$ PCE bands even at 500K [60]. When we compare the PCE intensity of the YSAGG samples with different Ga content at the same temperature, the PCE intensity increases with increasing Ga content. Thus, it is clear that the Ga-substituted $Y_3Sc_2Al_{3-x}Ga_xO_{12}:Ce^{3+}$ undergoes the thermal ionization quenching. With the same experimental setup, Lesniewski and our group also investigated the PCE spectra of $Gd_3Al_2Ga_3O_{12}$ and $Gd_3Ga_5O_{12}$ samples as shown in Fig. 23b and c [117], respectively. These two garnet phosphors also show strong $5d_1$ and $5d_2$ PCE bands and specific temperature dependence, which also demonstrate the thermal ionization quenching in the $Gd_3Al_2Ga_3O_{12}$ host and the auto-ionization in the $Gd_3Ga_5O_{12}$ host as observed in the similar hosts of $Y_3Al_2Ga_3O_{12}$ and $Y_3Ga_5O_{12}$. Based on the photoconductivity measurement in the series of Ce^{3+}-doped YAGG,

GAGG and YSAGG with Ga-substituted composition, the main quenching process was determined as the auto-ionization or the thermal ionization process.

3.3. Thermal ionization: thermoluminescence measurements

While we could demonstrate the thermal ionization process by the photoconductivity measurement, we still could not demonstrate the quenching process of YAG:Ce^{3+} having a quite high quantum efficiency at ambient temperature and the difficulty of photoconductivity measurement even at very high temperatures. In addition, phosphors for wLEDs are generally powder form, so that the photoconductivity measurement, which requires the samples with single crystal or ceramic forms, is not a conventional method. In 2015, we successfully demonstrated the thermal ionization process of YAG:Ce^{3+} by investigating the electrons moving from the excited 5d level of Ce^{3+} ion to the electron traps through the conduction band using thermoluminescence(TL) phenomenon [118]. Thermoluminescence and persistent luminescence (thermoluminescence at ambient temperature) are caused by detrapping of the charges that were previously trapped followed by recombination on a luminescent center. Charge trapping occurs when electrons in the excited state of luminescence centers are transferred to the CB (e.g. through thermal ionization) and then captured by traps in the host. By measuring the TL intensity or persistent luminescence (PersL) intensity as a function of the charging wavelength, the TL excitation (TLE) spectrum or the PersL excitation (PersLE) spectrum are obtained. Both of TLE [118] and PersLE [119] provide the information of the threshold energy for the photoionization process as obtained in the PCE spectrum [112]. The advantage for the TLE and the PersLE measurements is to be able to measure the powder samples.

Fig. 24a shows the TLE spectra of storage and persistent phosphors of $Y_3Al_{5-x}Ga_xO_{12}$: Ce^{3+}-Cr^{3+} with x = 0, 1, 2, 2.5 and 3, which we developed [41]. In these phosphors, Cr^{3+} acts as an efficient electron trap, so that the intense TL intensity can be observed above ambient temperature. Thus, the TLE spectra can be measured as shown in Fig. 24a. The samples were charged at ambient temperature by monochromatic light at each wavelength. The TLE spectrum of
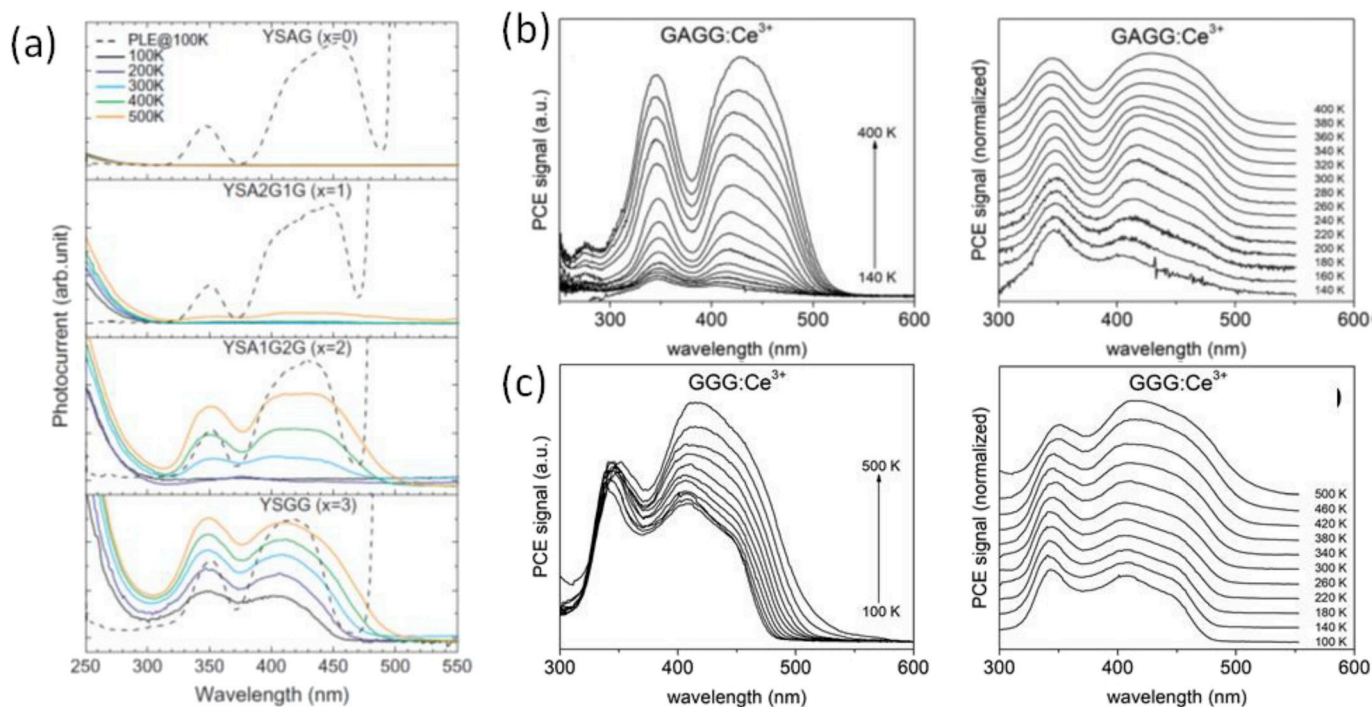

Fig. 23. Temperature variation of photocurrent excitation spectrum of (a) $Y_3Sc_2Al_{3-x}Ga_xO_{12}$ [60], (Reproduced with permission from Ref. [60], copyright 2013, Elsevier), (b) $Gd_3Al_2Ga_3O_{12}$ and (c) $Gd_3Ga_5O_{12}$ [117] (Reproduced from Ref. [117] with permission from the Royal Society of Chemistry).
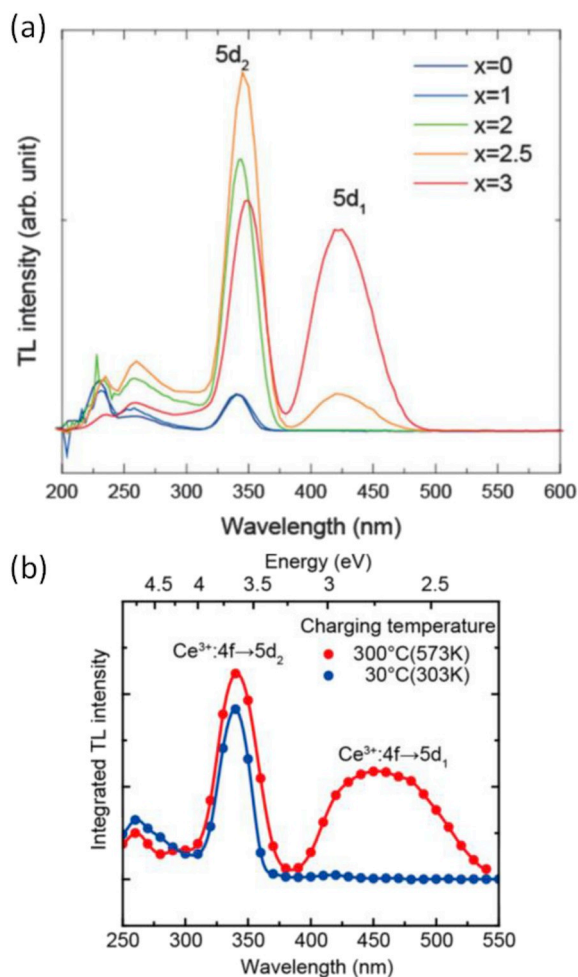
Fig. 24. (a) TLE spectra of $Y_3Al_{5-x}Ga_xO_{12}:Ce^{3+}-Cr^{3+}$ charged at ambient temperature [41]. (Reproduced from Ref. [41] with permission from the Royal Society of Chemistry). (b) TLE spectra of YAG:Ce^{3+} charged at 303 and 573 K [118] (Reproduced with permission from Ref. [118], copyright 2015, American Chemical Society).

$Y_3Al_2Ga_3O_{12}$: $Ce^{3+}-Cr^{3+}$ (Fig. 24a) is very similar to the PCE spectrum of $Y_3Al_2Ga_3O_{12}:Ce^{3+}$ (Fig. 21) at ambient temperature. From this accordance, it is possible to conclude that the effect by Cr^{3+} co-doping for the charging process is limited and the charging process is mainly determined by the energy location between the Ce^{3+}:$5d$ energy levels and the bottom of CB. Based on the TLE spectra charged at ambient temperature, it is found that the thermal ionization process from the $5d_1$ excited level to the bottom of CB occurs only in x = 3 and 2.5 samples at ambient temperature, but not in x = 0, 1 and 2. These results are in good agreement with the results of PL intensity as a function of temperature as shown in Fig. 19. The samples with x = 0, 1 and 2 do not show luminescence quenching at 300K, while the samples with x = 2.5 and 3 show clear quenching. Therefore, it is concluded that the TLE spectrum is very effective analysis to investigate the thermal ionization quenching.

The TLE spectrum analysis was also applied to the discussion of the luminescence quenching at higher temperatures for YAG:Ce^{3+} [118]. Fig. 24b shows the TLE spectra of a YAG:Ce^{3+} sample charged at 303 and 573 K, which are the temperatures that the YAG:Ce^{3+} sample does not show quenching and show quenching, respectively (Fig. 19). At 303 K, a TLE band is observed at around 340 nm while at 573 K an additional TLE band is observed at around 450 nm. The TLE bands at 450 nm and 340 nm are attributed to the transition from the $4f$ ground level to the $5d1$ and the $5d_2$, respectively. Because the trap filling

proceeds by the electron transport through the conduction band, these results provide the evidence that the electrons in the $5d_2$ level are thermally ionized to the conduction band already at 303 K but the electrons at the $5d_1$ level are only thermally ionized efficiently at higher temperatures around 573 K. At 573 K, a temperature corresponding to the onset of thermal quenching of the Ce^{3+} luminescence in the YAG:Ce^{3+} sample, the excitation in the lowest $5d_1$ band at 450 nm gives rise to a TL signal, indicating that the thermal ionization is responsible for the thermal quenching of the Ce^{3+} luminescence in the YAG host [118].

3.4. VRBE diagram and thermal ionization quenching

It is shown that the main quenching mechanism of some Ce^{3+}-doped garnets is caused by the thermal ionization. Its activation energy can be determined by the energy gap between the bottom of CB and the lowest $5d_1$ energy level. In this section, we discuss the thermal quenching behavior from the $Ln^{2+/3+}$-vacuum referred biding energy (VRBE) diagram which includes the valence band, conduction band and $Ln^{2+/3+}$ ground and excited levels. The $Ln^{2+/3+}$-VRBE can be constructed by spectroscopic data such as host exciton, charge transfer energy in Eu^{3+}-doped compound, red shift parameter of Ce^{3+} $D(1, 3+, A)$ and the Coulomb correlation energy $U(6,A)$, which is the energy difference between the ground state (GS) energy of Eu^{2+} and that of Eu^{3+} [52,120], without using the activation energy of the thermal ionization process. Therefore, the quenching process can be discussed by another approach using the energy gap between $5d_1$ and CB obtained by the VRBE diagram.

The VRBE of Eu^{2+} ($E_{4f}(7,2+,A)$) can be estimated by following eauation [121],

$$E_{4f}(7,2+,A) = -24.92 + \frac{18.05 - U(6,A)}{0.777 - 0.0353 U(6,A)} \quad (14)$$

Also, Dorenbos reported the correlation between $U(6,A)$ and ε_c of Ce^{3+} ion as below [122],

$$U(6,A) = 5.44 + 2.834 exp(-\varepsilon_c/2.2) \quad (15)$$

Thus, using equations (14) and (15), the VRBE of Eu^{2+} can be determined. Also the VRBE of Eu^{3+} can be determined from $U(6, A)$. After determining the VRBE of Eu^{2+}, the VRBE of valence band (VB) top can be estimated by the charge transfer (CT) energy of Eu^{3+} because the CT energy is equivalent to the energy gap between the top of the VB and the Eu^{2+} GS. After that the CB bottom can be determined from the band gap. In this study, the band gap energy at low temperature (~10K) is estimated from the creation energy of host exciton (E^{ex}) at low temperature using the $E^{ex} + 0.008(E^{ex})^2$ equation for correction of electron-hole binding energy [123]. If only the host exciton energy at room temperature was obtained, 0.15 eV was added to correct the factor by temperature.

Until now, the VRBE diagrams of garnet hosts have been reported, but the $U(6,A)$ value is often assumed as a constant in the series of garnets [41,57]. As shown in Chapter 2, it is clear that the Ce^{3+} centroid shift energy depends on the garnet host composition. Thus, different $U(6,A)$ should be used for each garnet composition. Using the empirical equations (2), (7) and (15), the $U(6,A)$ can be estimated from the garnet composition and the crystal structural data. However, the crystal structure data of garnet solid solutions such as $Gd_3Al_{5-x}Ga_xO_{12}$ with x = 1, 2, 3, 4, $Y_3Sc_2Al_{3-x}Ga_xO_{12}$ with x = 1 and 2, and $Gd_{3-y}Y_yAl_5O_{12}$ with y = 1, 2 have never reported. In these solid solutions, R_i in equation (2) cannot be obtained, so that $U(6,A)$ of these compounds were predicted by assuming that the $U(6,A)$ follows to the linear trend obtained from the data of end members. Also, the charge transfer energies in the $Y_3Sc_2Al_2Ga_1O_{12}$ and $Y_3Sc_2Al_1Ga_2O_{12}$ hosts were estimated based on the linear trend of CT energies of $Y_3Sc_2Al_3O_{12}$ and $Y_3Sc_2Ga_3O_{12}$ which are estimated from the Yb^{3+} charge transfer (private data). The collected parameters were shown in Table 3 and the

Table 3
Experimental data on exciton energy (E^{ex}), charge transfer (E^{CT}), U(6, A), D(1,3+,A), $\Delta E_{5d\text{-}CB}$ and $T_{50\%}$ in each garnet host.

Host, A	E^{ex} (eV)	Ref.	E^{CT} (eV)	Ref.	U(6,A) (eV)	D(1, 3+, A) (eV)	$\Delta E_{5d1\text{-}CB}$ (eV)	$T_{50\%}$ (K)	Ref.
$Gd_3Al_5O_{12}$	6.39	[55]	5.37	[25]	7.23	3.48	0.87	405	[55]
$Gd_3Al_4Ga_1O_{12}$	6.35	[57]	5.36	[57]	7.17	3.42	0.56	406	[55]
$Gd_3Al_3Ga_2O_{12}$	6.30	[57]	5.27	[57]	7.10	3.35	0.46	410	[55]
$Gd_3Al_2Ga_3O_{12}$	6.22	[57]	5.20	[57]	7.04	3.31	0.27	320	[55]
$Gd_3Al_1Ga_4O_{12}$	6.00	[57]	5.00	[57]	6.97	3.28	0.21	175	[55]
$Gd_3Ga_5O_{12}$	5.40	[55]	5.00	[126]	6.91	3.22	−0.15	< 10	[55]
$Gd_2Y_1Al_5O_{12}$	6.39	[57]	5.50	[57]	7.08	3.47	0.58	408	[127]
$Gd_1Y_2Al_5O_{12}$	6.54	[57]	5.60	[57]	6.94	3.45	0.49	454	[127]
$Y_3Al_5O_{12}$	7.10	[41]	5.42	[128]	6.79	3.41	1.09	640	[41]
$Y_3Al_4Ga_1O_{12}$	7.09	[41]	5.34	[41,128]	6.72	3.39	1.07	583	[41]
$Y_3Al_3Ga_2O_{12}$	6.88	[41]	5.25	[128]	6.68	3.34	0.84	491	[41]
$Y_3Al_2Ga_3O_{12}$	6.67	[41]	5.19	[128]	6.63	3.27	0.55	344	[41]
$Y_3Al_1Ga_4O_{12}$	6.42	[41]	5.12	[128]	6.60	3.24	0.05	301	[41]
$Y_3Ga_5O_{12}$	6.06	[41]	5.05	[128]	6.57	3.14	−0.16	< 10	[41]
$Lu_3Al_5O_{12}$	7.35	[25,114,129]	5.65	[130,131]	6.79	3.35	1.07	800	[22]
$Lu_3Ga_5O_{12}$	6.00	[129]	5.00	[132]	6.57	3.08	−0.23	< 10	[18,114,124]
$Y_3Sc_2Al_3O_{12}$	6.78	This work	5.13	This work	6.71	3.32	0.86	533	[60]
$Y_3Sc_2Al_2Ga_1O_{12}$	6.67	This work	5.07	This work	6.67	3.22	0.66	483	[60]
$Y_3Sc_2Al_1Ga_2O_{12}$	6.29	This work	5.02	This work	6.62	3.17	0.20	410	[60]
$Y_3Sc_2Ga_3O_{12}$	6.17	This work	4.96	This work	6.57	3.16	0.07	332	[60]
$Ca_3Sc_2Si_3O_{12}$	6.81	[82]	4.86	[82]	7.02	3.25	1.40	900	[23]
$Ca_3Y_2Ge_3O_{12}$	6.59	[70]	4.77	[70]	6.79	3.20	0.98	265	[70]
$Sr_3Y_2Ge_3O_{12}$	5.90	[70]	4.43	[70]	6.79	3.26	0.63	320	[23]
$Mg_3Y_2Ge_3O_{12}$	5.90	[74]	4.61	[133]	6.80	3.20	0.40	283	[75]

VRBE diagram was constructed as shown in Fig. 25.

Compared with the reported VRBE diagrams of garnet hosts [25,41], the relationship between the 5d energy levels and the CB bottom was changed and new VRBE diagrams are more reasonable. For instance, in the previous VRBE diagram of Ce^{3+}-doped LuGG, GGG and YGG, the $5d_1$ energy is lower than the bottom of CB [25], which implies that the luminescence can be observed at low temperature. However, these Ce^{3+}-doped LuGG, GGG and YGG do not show the luminescence even at low temperatures [55,112,124]. In the new VRBE diagram, the $5d_1$ energy in these hosts is completely located within the conduction band which is the same situation as predicted from the photo-conductivity measurement [112]. From the obtained VRBE diagram, the energy gap between $5d_1$ and CB bottom ($\Delta E_{5d1\text{-}CB}$) was summarized as shown in column 5 of Table 3. The $T_{50\%}$ is also shown in column 6 of Table 3.

Fig. 26 shows the $T_{50\%}$ quenching temperature as a function of $\Delta E_{5d1\text{-}CB}$. If the quenching process is the thermal ionization, the quenching temperature is related to the energy gap of $\Delta E_{5d1\text{-}CB}$. In actual, the $T_{50\%}$ increases with increasing $\Delta E_{5d1\text{-}CB}$ (Fig. 26). From the $T_{50\%} = \frac{\Delta E}{k \times ln\left(\frac{\Gamma_0}{\Gamma_v}\right)}$, see Eq. (13), the linear trend is expected in Fig. 26. The typical radiative rate for Ce^{3+} is roughly estimated to be 2×10^7 s^{-1}, which corresponds to approximately 50 ns radiative lifetime. The typical phonon frequency of oxide compounds are 500–1000 cm^{-1}, so that Γ_0 in oxide material is typically ~2×10^{13} s^{-1} [125]. The Boltzmann constant is 8.617×10^{-5} eV/K. Based on these parameters and Eq. (13), one obtains $T_{50\%} = 840\Delta E$ in eV unit. The experimental $T_{50\%}$ values against $\Delta E_{5d1\text{-}CB}$ were fitted by a linear function, resulting in the slope of 620 K/eV. For the fitting, unreliable and non-luminescent Ce^{3+}-doped GGG, LuGG, YGG data were excluded. The
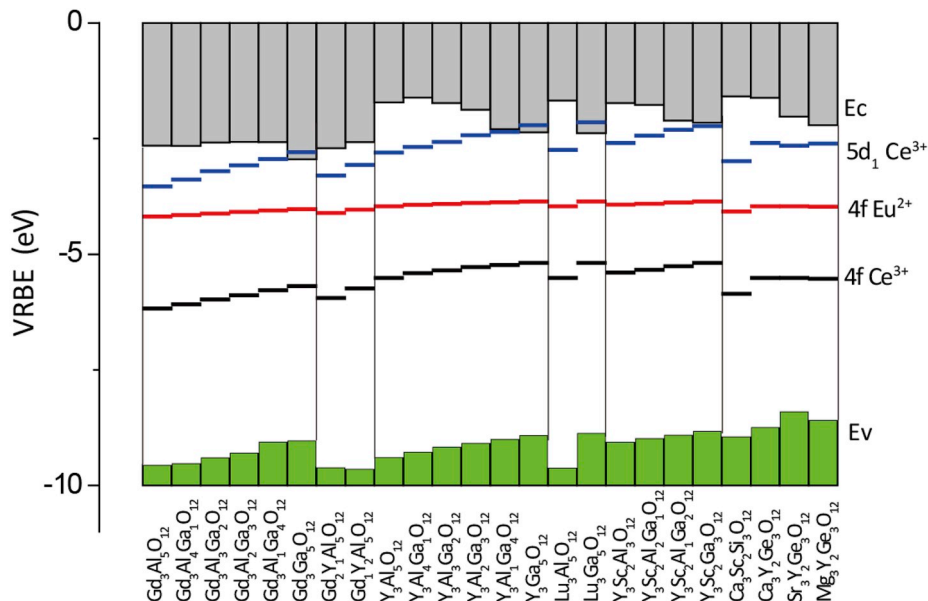

Fig. 25. Stacked VRBE diagram of garnet hosts using various U(6,A) parameter which was obtained from the centroid shift estimated by optical basicity.
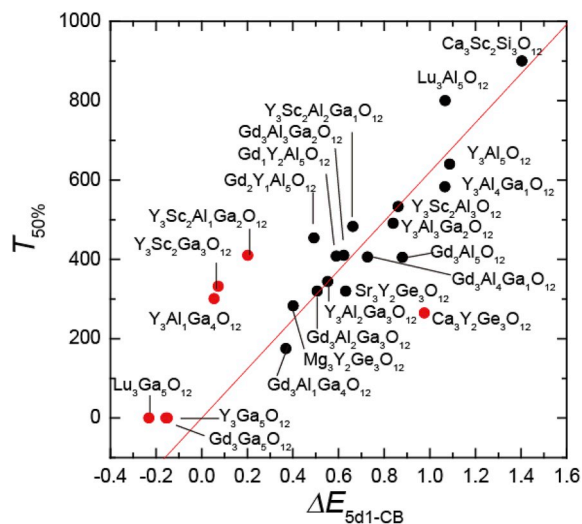
京都大学
KYOTO UNIVERSITY

J. Ueda and S. Tanabe

Optical Materials: X 1 (2019) 100018

京都大学学術情報リポジトリ
KURENAI 紅
Kyoto University Research Information Repository

Fig. 26. Quenching temperature of $T_{50\%}$ against $\Delta E_{5d\text{-CB}}$ estimated from the VRBE diagram. Red line is a linear fitting result. (For interpretation of the references to color in this figure legend, the reader is referred to the Web version of this article.)

experimental slope shows good agreement with the theoretical value. Based on the linearity and the agreement of experimental and theoretical slopes in the plot of $T_{50\%}$ against $\Delta E_{5d1\text{-CB}}$ in Fig. 26, it is suggested that the luminescence quenching of the Ce^{3+}-doped garnets is caused by the thermal ionization process. In conclusion, based on the experimental results, such as photoconductivity and thermoluminescence, and the energy diagram, we conclude that the most probable quenching process is the thermal ionization process in almost every Ce^{3+}-doped garnet.

4. Conclusion

In the introduction, the optical applications of Ce^{3+}-doped garnets, the (local) crystal structure and the general luminescent properties of Ce^{3+} were summarized. In Chapter 2, the centroid shift and the crystal field splitting of Ce^{3+}:5d state in garnets were discussed. From the collected all of 5d energy levels in nine garnets, it is found that the centroid shift energy of Ce^{3+} ion in various garnets are different from each other. The spectroscopic polarizability, which is correlated with the centroid shift energy, shows a linear trend against optical basicity. The crystal field splitting between the lowest $5d_1$ and the highest $5d_5$ (ε_{cfs}) is found to be correlated with the crystal filed splitting between $5d_1$ and $5d_2$ (Δ_{12}). Also, it is observed that Δ_{12} shows a linear trend with respect to a new disordered parameter which is defined by $d_{83}/(d_{48} \cdot R_{av})$. Based on these trends, the empirical equations were obtained to predict the centroid shift, Δ_{12} and ε_{cfs} from the composition and crystal structure data.

In Chapter 3, the quenching mechanisms of thermally activated crossover and thermal ionization were summarized. The experimental data of the quantum yield and the temperature dependence of photoluminescence intensity in Ce^{3+}-doped rare earth aluminum gallium garnets were introduced. Subsequently, the decrease of QY at ambient temperature and the decrease of quenching temperature ($T_{50\%}$) were reported with increasing Ga content. Based on the photocurrent excitation (PCE) measurement, the electron transfer process from Ce^{3+} to the conduction band was indicated directly in the series of Ce^{3+}-doped garnets. Another experimental method of thermoluminescence excitation (TLE) spectrum and its experimental results are introduced to demonstrate the thermal ionization process. It was shown that the TLE spectrum is a conventional and powerful tool to check the thermal ionization process. The thermal ionization process depends on the energy gap between the $5d_1$ level and the bottom of the conduction band

($\Delta E_{5d1\text{-CB}}$), so that the correlation between $T_{50\%}$ and $\Delta E_{5d1\text{-CB}}$ were investigated. The $\Delta E_{5d1\text{-CB}}$ was estimated from the constructed vacuum referred binding energy (VRBE) diagram which takes into account different $U(6,A)$ value for each garnet. The linear trend was observed in the plot of $T_{50\%}$ against $\Delta E_{5d1\text{-CB}}$ in Ce^{3+}-doped garnets, which shows that the main luminescence quenching of all of Ce^{3+}-doped garnets is due to the thermal ionization.

Declaration of interests

The authors declare that they have no known competing financial interests or personal relationships that could have appeared to influence the work reported in this paper.

References

[1] G. Blasse, A. Bril, A new phosphor for flying-spot cathode-ray tubes for color television: yellow-emitting $Y_3Al_5O_{12}$–Ce^{3+}, Appl. Phys. Lett. 11 (1967) 53–55.

[2] P. Schauer, R. Autrata, Electro-optical properties of a scintillation detector in SEM, J. Microsc. Spectrosc. Electron. 4 (1979) 633–650.

[3] M. Moszyński, T. Ludziejewski, D. Wolski, W. Klamra, L.O. Norlin, Properties of the YAG:Ce scintillator, Nucl. Instrum. Methods Phys. Res., Sect. A 345 (1994) 461–467.

[4] M. Weber, S. Derenzo, C. Dujardin, W. Moses, Dense Ce^{3+}-activated scintillator materials, Proceedings of SCINT1995, pp. 325-328.

[5] M. Nikl, E. Mihoková, J.A. Mareš, A. Vedda, M. Martini, K. Nejezchleb, K. Blažek, Traps and timing characteristics of LuAG:Ce^{3+} scintillator, Phys. Status Solidi 181 (2000) R10–R12.

[6] K. Bando, K. Sakano, Y. Noguchi, Y. Shimizu, Development of high-bright and pure-white LED lamps, J. Light Vis. Environ. 22 (1998) 2–4.

[7] S. Nishiura, S. Tanabe, K. Fujioka, Y. Fujimoto, Properties of transparent Ce:YAG ceramic phosphors for white LED, Opt. Mater. 33 (2011) 688–691.

[8] S. Nishiura, S. Tanabe, K. Fujioka, Y. Fujimoto, Preparation of transparent Ce^{3+}:GdYAG ceramics phosphors for white LED, IOP Conf. Ser. Mater. Sci. Eng. 18 (2011) 102005.

[9] J. Ueda, S. Tanabe, Visible to near infrared conversion in Ce^{3+}-Yb^{3+} Co-doped YAG ceramics, J. Appl. Phys. 106 (2009) 043101.

[10] J. Ueda, K. Aishima, S. Nishiura, S. Tanabe, Afterglow luminescence in Ce^{3+}-doped $Y_3Sc_2Ga_3O_{12}$ ceramics, APEX 4 (2011) 042602.

[11] J. Ueda, K. Kuroishi, S. Tanabe, Bright persistent ceramic phosphors of Ce^{3+}-Cr^{3+}-codoped garnet able to store by blue light, Appl. Phys. Lett. 104 (2014) 101904.

[12] H. Lin, B. Wang, J. Xu, R. Zhang, H. Chen, Y. Yu, Y. Wang, Phosphor-in-Glass for high-powered remote-type white AC-LED, ACS Appl. Mater. Interfaces 6 (2014) 21264–21269.

[13] H. Lin, J. Xu, Q. Huang, B. Wang, H. Chen, Z. Lin, Y. Wang, Bandgap tailoring via Si doping in inverse-garnet $Mg_3Y_2Ge_3O_{12}$:Ce^{3+} persistent phosphor potentially applicable in AC-LED, ACS Appl. Mater. Interfaces 7 (2015) 21835–21843.

[14] K. Asami, J. Ueda, S. Tanabe, Flicker suppression of AC driven white LED by yellow persistent phosphor of Ce^{3+}–Cr^{3+} Co-doped garnet, Journal of Science and Technology in Lighting 41 (2018) 89–92.

[15] Z. Xia, A. Meijerink, Ce^{3+}-Doped garnet phosphors: composition modification, luminescence properties and applications, Chem. Soc. Rev. 46 (2017) 275–299.

[16] Y.-C. Lin, M. Karlsson, M. Bettinelli, Inorganic phosphor materials for lighting, Top. Curr. Chem. 374 (2016) 1–47.

[17] M. Nikl, A. Yoshikawa, K. Kamada, K. Nejezchleb, C.R. Stanek, J.A. Mares, K. Blazek, Development of LuAG-based scintillator crystals – a review, Prog. Cryst. Growth Char. Mater. 59 (2013) 47–72.

[18] K. Kamada, T. Endo, K. Tsutumi, T. Yanagida, Y. Fujimoto, A. Fukabori, A. Yoshikawa, J. Pejchal, M. Nikl, Composition engineering in cerium-doped $(Lu,Gd)_3(Ga,Al)_5O_{12}$ single-crystal scintillators, Cryst. Growth Des. 11 (2011) 4484–4490.

[19] N.J. Cherepy, Z.M. Seeley, S.A. Payne, P.R. Beck, O.B. Drury, S.P.O. Neal, K.M. Figueroa, S. Hunter, L. Ahle, P.A. Thelin, T. Stefanik, J. Kindem, Development of transparent ceramic Ce-doped gadolinium garnet gamma spectrometers, IEEE Trans. Nucl. Sci. 60 (2013) 2330–2335.

[20] T. Yanagida, K. Kamada, Y. Fujimoto, H. Yagi, T. Yanagitani, Comparative study of ceramic and single crystal Ce:GAGG scintillator, Opt. Mater. 35 (2013) 2480–2485.

京都大学
KYOTO UNIVERSITY

[21] V. Bachmann, C. Ronda, A. Meijerink, Temperature quenching of yellow Ce^{3+} luminescence in YAG:Ce, Chem. Mater. 21 (2009) 2077–2084.

[22] K.V. Ivanovskikh, J.M. Ogiegło, A. Zych, C.R. Ronda, A. Meijerink, Luminescence temperature quenching for Ce^{3+} and Pr^{3+} d-f emission in YAG and LuAG, ECS J. Solid. State Sci. Technol. 2 (2013) R3148–R3152.

[23] S.K. Sharma, Y.-C. Lin, I. Carrasco, T. Tingberg, M. Bettinelli, M. Karlsson, Weak thermal quenching of the luminescence in the $Ca_3Sc_2Si_3O_{12}$:Ce^{3+} garnet phosphor, J. Mater. Chem. C 6 (2018) 8923–8933.

[24] P. Dorenbos, 5d-level energies of Ce^{3+} and the crystalline environment. IV. Aluminates and "simple" oxides, J. Lumin. 99 (2002) 283–299.

[25] P. Dorenbos, Electronic structure and optical properties of the lanthanide activated $RE_3(Al_{1-x}Ga_x)_5O_{12}$ (RE=Gd, Y, Lu) garnet compounds, J. Lumin. 134 (2013) 310–318.

[26] A.A. Setlur, Phosphors for LED-based solid-state lighting, J. Electrochem. Soc. Interface 18 (2009) 32–36.

[27] C.C. Lin, R.-S. Liu, Advances in phosphors for light-emitting diodes, J. Phys. Chem. Lett. 2 (2011) 1268–1277.

[28] S. Park, T. Vogt, Defect monitoring and substitutions in $Sr_{3-x}A_xAlO_4F$ (A = Ca, Ba) oxyfluoride host lattices and phosphors, J. Phys. Chem. C 114 (2010) 11576–11583.

[29] T.-G. Kim, T. Kim, J. Kim, S.-J. Kim, S.-J. Im, Interplay between crystal structure and photoluminescence properties of β-$Ca_3SiO_4Cl_2$:Eu^{2+}, J. Phys. Chem. C 118 (2014) 12428–12435.

[30] W. Lv, Y. Jia, Q. Zhao, W. Lü, M. Jiao, B. Shao, H. You, Synthesis, structure, and luminescence properties of $K_2Ba_7Si_{16}O_{40}$:Eu^{2+} for white light emitting diodes, J. Phys. Chem. C 118 (2014) 4649–4655.

[31] Z. Xia, Y. Zhang, M.S. Molokeev, V.V. Atuchin, Structural and luminescence properties of yellow-emitting $NaScSi_2O_6$:Eu^{2+} phosphors: Eu^{2+} site preference analysis and generation of red emission by codoping Mn^{2+} for white-light-emitting diode applications, J. Phys. Chem. C 117 (2013) 20847–20854.

[32] C.C. Chiang, M.S. Tsai, M.H. Hon, Luminescent properties of cerium-activated garnet series phosphor: structure and temperature effects, J. Electrochem. Soc. 155 (2008) 517–520.

[33] T.Y. Tien, E.F. Gibbons, R.G. DeLosh, P.J. Zacmanidis, D.E. Smith, H.L. Stadler, Ce^{3+} activated $Y_3Al_5O_{12}$ and some of its solid solutions, J. Electrochem. Soc. 120 (1973) 278–281.

[34] J.L. Wu, G. Gundiah, A.K. Cheetham, Structure-property correlations in Ce-doped garnet phosphors for use in solid state lighting, Chem. Phys. Lett. 441 (2007) 250–254.

[35] Z. Song, Z. Xia, Q. Liu, Insight into the relationship between crystal structure and crystal-field splitting of Ce^{3+} doped garnet compounds, J. Phys. Chem. C 122 (2018) 3567–3574.

[36] L. Seijo, Z. Barandiarán, Host effects on the optically active 4f and 5d levels of Ce^{3+} in garnets, PCCP 15 (2013) 19221–19231.

[37] C. Struck, W. Fonger, Understanding Luminescence Spectra and Efficiency Using W P and Related Functions, Springer Berlin Heidelberg, Berlin, Germany, 1991.

[38] G. Blasse, W. Schipper, J.J. Hamelink, On the quenching of the luminescence of the trivalent cerium ion, Inorg. Chim. Acta 189 (1991) 77–80.

[39] W.W. Holloway Jr., M. Kestigian, On the fluorescence of cerium-activated garnet crystals, Phys. Lett. 25 (1967) 614–615.

[40] J.W.W. Holloway, M. Kestigian, Optical properties of cerium-activated garnet crystals, J. Opt. Soc. Am. 59 (1969) 60–63.

[41] J. Ueda, P. Dorenbos, A.J.J. Bos, K. Kuroishi, S. Tanabe, Control of electron transfer between Ce^{3+} and Cr^{3+} in the $Y_3Al_{5-x}Ga_xO_{12}$ host via conduction band engineering, J. Mater. Chem. C 3 (2015) 5642–5651.

[42] S. Nishikawa, Crystal structure of a garnet, Tokyo Sugaku-Buturigakkwai Kizi Dai 2 Ki 9 (1917) 194–197.

[43] G. Menzer, XX. Die Kristallstruktur der Granate, Zeitschrift für Kristallographie - Crystalline Materials 1929, pp. 300.

[44] H.W. Jaffe, The role of yttrium and other minor elements in the garnet group 1, Am. Mineral. 36 (1951) 133–155.

[45] H.S. Yoder, M.L. Keith, COMPLETE SUBSTITUTION OF ALUMINUM FOR SILICON - THE SYSTEM - 3MnO·Al_2O_3·3SiO_2-3Y_2O_3·5Al_2O_3, Am. Mineral. 36 (1951) 519–533.

[46] F. Euler, J.A. Bruce, Oxygen coordinates of compounds with garnet structure, Acta Crystallogr. 19 (1965) 971–978.

[47] A. Nakatsuka, A. Yoshiasa, S. Takeno, Site preference of cations and structural variation in $Y_3Fe_{5-x}Ga_xO_{12}$ (0 < = x < = 5) solid solutions with garnet structure, Acta Crystallogr. B 51 (1995) 737–745.

[48] R.J. Lang, THE SPECTRUM OF TREBLY IONIZED CERIUM, Can. J. Res. 14a (1936) 127–130.

[49] P. Dorenbos, 5d-level energies of Ce^{3+} and the crystalline environment. I. Fluoride compounds, Phys. Rev. B 62 (2000) 15640–15649.

[50] P. Dorenbos, 5d-level energies of Ce^{3+} and the crystalline environment. II. Chloride, bromide, and iodide compounds, Phys. Rev. B 62 (2000) 15650–15659.

[51] P. Dorenbos, 5d-level energies of Ce^{3+} and the crystalline environment. III. Oxides containing ionic complexes, Phys. Rev. B 64 (2001).

[52] P. Dorenbos, A review on how lanthanide impurity levels change with chemistry and structure of inorganic compounds, ECS J. Solid. State Sci. Technol. 2 (2013) R3001–R3011.

[53] P.D. Rack, P.H. Holloway, The structure, device physics, and material properties of thin film electroluminescent displays, Mater. Sci. Eng. R Rep. 21 (1998) 171–219.

[54] Clarendon B. Henderson, G.F. Imbusch, Optical Spectroscopy of Inorganic Solids, Press, 2006.

[55] J.M. Ogiegło, A. Katelnikovas, A. Zych, T. Jüstel, A. Meijerink, C.R. Ronda, Luminescence and luminescence quenching in $Gd_3(Ga,Al)_5O_{12}$ scintillators doped with Ce^{3+}, J. Phys. Chem. A 117 (2013) 2479–2484.

[56] A.C. Sackville Hamilton, G.I. Lampronti, S.E. Rowley, S.E. Dutton, Enhancement of the magnetocaloric effect driven by changes in the crystal structure of Al-doped GGG, $Gd_3Ga_{5-x}Al_xO_{12}$(0 ≤ x ≤ 5), J. Phys. Condens. Matter 26 (2014) 116001.

[57] K. Asami, J. Ueda, M. Kitaura, S. Tanabe, Investigation of luminescence quenching and persistent luminescence in Ce^{3+} doped (Gd,Y)$_3$(Al,Ga)$_5O_{12}$ garnet using vacuum referred binding energy diagram, J. Lumin. 198 (2018) 418–426.

[58] J. Ueda, K. Kuroishi, S. Tanabe, Development of blue excitable persistent phosphor of Ce^{3+}-doped garnet ceramics by bandgap engineering and metal sensitization, Proc. SPIE 8987, Oxide-Based Materials and Devices V, 8987, 2014, pp. 1–7.

[59] A. Nakatsuka, A. Yoshiasa, T. Yamanaka, Cation distribution and crystal chemistry of $Y_3Al_{5-x}Ga_xO_{12}$ (0 < = x < = 5) garnet solid solutions, Acta Crystallogr. B 55 (1999) 266–272.

[60] J. Ueda, K. Aishima, S. Tanabe, Temperature and compositional dependence of optical and optoelectronic properties in Ce^{3+}-doped $Y_3Sc_2Al_{3-x}Ga_xO_{12}$ (x=0, 1, 2, 3), Opt. Mater. 35 (2013) 1952–1957.

[61] Y. Luo, Z. Xia, Effect of Al/Ga substitution on photoluminescence and phosphorescence properties of garnet-type $Y_3Sc_2Ga_{3-x}Al_xO^{12}$:$Ce^{3+}$ phosphor, J. Phys. Chem. C 118 (2014) 23297–23305.

[62] T.H. Allik, C.A. Morrison, J.B. Gruber, M.R. Kokta, Crystallography, spectroscopic analysis, and lasing properties of Nd^{3+}:$Y_3Sc_2Al_3O_{12}$, Phys. Rev. B 41 (1990) 21–30.

[63] V.A. Efremov, N.D. Zakharov, G.M. Kuz'micheva, B.V. Mukhin, V.V. Chernyshev, Yttrium scandium-gallium garnet: crystal structure, Zhurnal Neorganicheskoj Khimii 38 (1993) 220–225.

[64] S. Yamazaki, F. Marumo, K. Tanaka, H. Morikawa, N. Kodama, K. Kitamura, Y. Miyazawa, A structural study of facet and off-facet parts of rare-earth garnets, $Gd_3Sc_2Al_3O_{12}$, $Gd_3Sc_2Ga_3O_{12}$, and $La_3Lu_2Ga_3O_{12}$, J. Solid State Chem. 108 (1994) 94–98.

[65] M. Kottaisamy, P. Thiyagarajan, J. Mishra, M.S. Ramachandra Rao, Color tuning of $Y_3Al_5O_{12}$:Ce phosphor and their blend for white LEDs, Mater. Res. Bull. 43 (2008) 1657–1663.

[66] M. Batentschuk, B. Schmitt, J. Schneider, A. Winnacker, Color engineering of garnet based phosphors for luminescence conversion light emitting diodes (lucoleds), MRS Proceedings 560 (2011) 215.

[67] Y. Zorenko, V. Gorbenko, T. Voznyak, M. Batentschuk, A. Osvet, A. Winnacker, Luminescence and Tb^{3+}–Ce^{3+}–Eu^{3+} ion energy transfer in single-crystalline films of $Tb_3Al_5O_{12}$:Ce,Eu garnet, J. Lumin. 128 (2008) 652–660.

[68] J. Hammann, Etude par diffraction de neutrons a 0,31degreesK de la structure antiferromagnetique des grenats d'aluminium-terbium et d'aluminium-holmium, Acta Crystallogr. B 25 (1969) 1853–1856.

[69] A. Kalaji, P.J. Saines, N.C. George, A.K. Cheetham, Photoluminescence of cerium-doped $(Ca_{1-x}Sr_x)_3RE_2Ge_3O_{12}$ garnet phosphors for solid state lighting: relating structure to emission, Chem. Phys. Lett. 586 (2013) 91–96.

[70] H. Luo, L. Ning, Y. Dong, A.J.J. Bos, P. Dorenbos, Electronic structure and site occupancy of lanthanide-doped (Sr, Ca)$_3$(Y, Lu)$_2Ge_3O_{12}$ garnets: a spectroscopic and first-principles study, J. Phys. Chem. C 120 (2016) 28743–28752.

[71] S.J. Marin, M. O'Keeffe, V.G. Young, R.B. Von Dreele, The crystal structure of $Sr_3Y_2Ge_3O_{12}$, J. Solid State Chem. 91 (1991) 173–175.

[72] D. Levy, J. Barbier, Normal and inverse garnets: $Ca_3Fe_2Ge_3O_{12}$, $Ca_3Y_2Ge_3O_{12}$ and $Mg_3Y_2Ge_3O_{12}$, Acta Crystallogr. C 55 (1999) 1611–1614.

[73] M.C. Dalconi, S. Quartieri, R. Oberti, M. Boiocchi, F. Boscherini, O. Safonova, A.B. Woodland, Site preference and local geometry of Sc in garnets: Part II. The crystal-chemistry of octahedral Sc in the andradite–$Ca_3Sc_2Si_3O_{12}$ join, Am. Mineral. 91 (2006) 1240–1248.

[74] Z. Jiang, Y. Wang, L. Wang, Enhanced yellow-to-orange emission of Si-doped $Mg_3Y_2Ge_3O_{12}$: Ce^{3+} garnet phosphors for warm white light-emitting diodes, J. Electrochem. Soc. 157 (2010) J155–J158.

[75] T. Shimizu, J. Ueda, S. Tanabe, Optical and optoelectronic properties of Ce^{3+} doped Mg_3Y_2(Ge,Si)$_3O_{12}$ inverse garnet, Phys. Stat. Sol. c 9 (2012) 2296–2299.

[76] Y. Zhou, W. Zhuang, Y. Hu, R. Liu, Z. Jiang, Y. Liu, Y. Li, Y. Zheng, L. Chen, J. Zhong, A broad-band orange-yellow-emitting $Lu_2Mg_2Al_2Si_2O_{12}$: Ce^{3+} phosphor for application in warm white light-emitting diodes, RSC Adv. 7 (2017) 46713–46720.

[77] A.A. Setlur, W.J. Heward, Y. Gao, A.M. Srivastava, R.G. Chandran, M.V. Shankar, Crystal chemistry and luminescence of Ce^{3+}-doped Lu_2CaMg_2(Si,Ge)$_3O_{12}$ and its use in LED based lighting, Chem. Mater. 18 (2006) 3314–3322.

[78] Y.V. Zorenko, V.I. Gorbenko, G.B. Stryganyuk, V.N. Kolobanov, D.A. Spasskii, K. Blazek, M. Nikl, Luminescence of excitons and antisite defects in $Lu_3Al_5O_{12}$:Ce single crystals and single-crystal films, Optic Spectrosc. 99 (2005) 923–931.

[79] T. Tomiki, H. Akamine, M. Gushiken, Y. Kinjoh, M. Miyazato, T. Miyazato, N. Toyokawa, M. Hiraoka, N. Hirata, Y. Ganaha, T. Futemma, Ce^{3+} centres in $Y_3Al_5O_{12}$ (YAG) single crystals, J. Phys. Soc. Jpn. 60 (1991) 2437.

[80] P.A. Tanner, L. Fu, L. Ning, B.-M. Cheng, M.G. Brik, Soft synthesis and vacuum ultraviolet spectra of YAG:Ce^{3+} nanocrystals: reassignment of Ce^{3+} energy levels, J. Phys. Condens. Matter 19 (2007) 216213.

[81] J.M. Ogiegło, A. Zych, K.V. Ivanovskikh, T. Jüstel, C.R. Ronda, A. Meijerink, Luminescence and energy transfer in Lu3Al5O12 scintillators Co-doped with Ce3 + and Tb3 +, J. Phys. Chem. A 116 (2012) 8464–8474.

[82] C.M. Wong, S.R. Rotman, C. Warde, Optical studies of cerium doped yttrium aluminum garnet single crystals, Appl. Phys. Lett. 44 (1984) 1038–1040.

[83] L. Zhou, W. Zhou, F. Pan, R. Shi, L. Huang, H. Liang, P.A. Tanner, X. Du, Y. Huang, Y. Tao, L. Zheng, Spectral properties and energy transfer of a potential solar energy converter, Chem. Mater. 28 (2016) 2834–2843.

[84] C.A. Morrison, Host dependence of the rare-earth ion energy separation $4f^N$–$4f^{N-1}$nl, J. Phys. Chem. 72 (1980) 1001–1002.

[85] P. Dorenbos, Relating the energy of the [Xe]5d^1 configuration of Ce^{3+} in inorganic compounds with anion polarizability and cation electronegativity, Phys. Rev. B 65 (2002) 235110.

[86] P. Dorenbos, Optical basicity, interpreted by means of Ce^{3+} 5d level spectroscopy in ionic crystals, J. Non-Cryst. Solids 324 (2003) 220–229.

[87] J.A. Duffy, M.D. Ingram, Use of thallium(I), lead(II), and bismuth(III) as spectro-scopic probes for ionic–covalent interaction in glasses, J. Phys. Chem. 52 (1970) 3752–3754.

[88] J.A. Duffy, M.D. Ingram, Establishment of an optical scale for Lewis basicity in inorganic oxyacids, molten salts, and glasses, J. Am. Chem. Soc. 93 (1971) 6448–6454.

[89] J.A. Duffy, M.D. Ingram, New correlation between s–p spectra and the nephe-lauxetic ratio β: applications in molten salt and glass chemistry, J. Phys. Chem. 54 (1971) 443–444.

[90] J.A. Duffy, M.D. Ingram, Optical basicity—IV: influence of electronegativity on the Lewis basicity and solvent properties of molten oxyanion salts and glasses, J. Inorg. Nucl. Chem. 37 (1975) 1203–1206.

[91] J.A. Duffy, M.D. Ingram, Nephelauxetic effect and Pauling electronegativity, J. Chem. Soc., Chem. Commun. (1973) 635–636.

[92] J.A. Duffy, Energy gaps, polarisation and partial metallic valence, Solid State Commun. 51 (1984) 429–431.

[93] V. Dimitrov, S. Sakka, Electronic oxide polarizability and optical basicity of simple oxides. I, J. Appl. Phys. 79 (1996) 1736–1740.

[94] J.A. Duffy, The electronic polarisability of oxygen in glass and the effect of com-position, J. Non-Cryst. Solids 297 (2002) 275–284.

[95] J.A. Duffy, Trends in energy gaps of binary compounds: an approach based upon electron transfer parameters from optical spectroscopy, J. Phys. C Solid State Phys. 13 (1980) 2979–2989.

[96] J.A. Duffy, Optical basicity analysis of glasses containing trivalent scandium, yt-trium, gallium and indium, Phys. Chem. Glasses 46 (2005) 500–504.

[97] P. Dorenbos, Crystal field splitting of lanthanide 4f$^{n−1}$5d-levels in inorganic compounds, J. Alloy. Comp. 341 (2002) 156–159.

[98] Y. Liu, J. Hao, W. Zhuang, Y. Hu, Structural and luminescent properties of gel-combustion synthesized green-emitting Ca$_3$Sc$_2$Si$_3$O$_{12}$: Ce^{3+}phosphor for solid-state lighting, J. Phys. D Appl. Phys. 42 (2009) 245102.

[99] G. Blasse, QUENCHING MECHANISMS OF Ce^{3+} LUMINESCENCE, in: P. Dorenbos, C.W.E.v. Eijk (Eds.), SCINT 95 : Proceedings of the International Conference on Inorganic Scintillators and Their Applications, Delft University Press, Delft, 1996.

[100] J. Ueda, A. Meijerink, P. Dorenbos, A.J.J. Bos, S. Tanabe, Thermal ionization and thermally activated crossover quenching processes for 5d-4f luminescence in Y$_3$Al$_{5-x}$Ga$_x$O$_{12}$:Pr^{3+}, Phys. Rev. B 95 (2017) 014303.

[101] W.M. Yen, M. Raukas, S.A. Basun, W. van Schaik, U. Happek, Optical and pho-toconductive properties of cerium-doped crystalline solids, J. Lumin. 69 (1996) 287–294.

[102] M. Raukas, S. Basun, W.M. Dennis, D.R. Evans, U. Happek, W. Van Schaik, W.M. Yen, Optical properties of Ce^{3+}-doped Lu$_2$O$_3$ and Y$_2$O$_3$ single crystals, J. Soc. Inf. Disp. 4 (1996) 189–192.

[103] M. Raukas, S.A. Basun, W. Van Schaik, W.M. Yen, U. Happek, Luminescence ef-ficiency of cerium doped insulators: the role of electron transfer processes, Appl. Phys. Lett. 69 (1996) 3300–3302.

[104] M. Nikl, A. Vedda, M. Fasoli, I. Fontana, V.V. Laguta, E. Mihokova, J. Pejchal, J. Rosa, K. Nejezchleb, Shallow traps and radiative recombination processes in Lu$_3$Al$_5$O$_{12}$:Ce single crystal scintillator, Phys. Rev. B 76 (2007) 195121.

[105] E. Mihóková, M. Nikl, J.A. Mareš, A. Beitlerová, A. Vedda, K. Nejezchleb, K. Blažek, C. D'Ambrosio, Luminescence and scintillation properties of YAG:Ce single crystal and optical ceramics, J. Lumin. 126 (2007) 77–80.

[106] M.J. Weber, Nonradiative decay from 5d states of rare earths in crystals, Solid State Commun. 12 (1973) 741–744.

[107] R.R. Jacobs, W.F. Krupke, M.J. Weber, Measurement of excited-state-absorption loss for Ce^{3+} in Y$_3$Al$_5$O$_{12}$ and implications for tunable 5d→4f rare-earth lasers, Appl. Phys. Lett. 33 (1978) 410–412.

[108] J.F. Owen, P.B. Dorain, T. Kobayasi, Excited-state absorption in Eu^{+2}: CaF2 and Ce^{+3}: YAG single crystals at 298 and 77 K, J. Appl. Phys. 52 (1981) 1216–1223.

[109] C. Pedrini, F. Rogemond, D.S. McClure, Photoionization thresholds of rare-earth impurity ions. Eu^{2+}:CaF$_2$, Ce^{3+}:YAG, and Sm^{2+}:CaF$_2$, J. Appl. Phys. 59 (1986) 1196–1201.

[110] L.-J. Lyu, D.S. Hamilton, Radiative and nonradiative relaxation measurements in Ce^{3+} doped crystals, J. Lumin. 48–49 (1991) 251–254.

[111] D.S. Hamilton, S.K. Gayen, G.J. Pogatshnik, R.D. Ghen, W.J. Miniscalco, Optical-absorption and photoionization measurements from the excited states of Ce^{3+}:Y$_3$Al$_5$O$_{12}$, Phys. Rev. B 39 (1989) 8807–8815.

[112] J. Ueda, S. Tanabe, T. Nakanishi, Analysis of Ce^{3+} luminescence quenching in solid solutions between Y$_3$Al$_5$O$_{12}$ and Y$_3$Ga$_5$O$_{12}$ by temperature dependence of photoconductivity measurement, J. Appl. Phys. 110 (2011) 053102.

[113] U. Happek, J. Choi, A.M. Srivastava, Observation of cross-ionization is Gd$_3$Sc$_2$Al$_3$O$_{12}$:Ce^{3+}, J. Lumin. 94–95 (2001) 7–9.

[114] M. Fasoli, A. Vedda, M. Nikl, C. Jiang, B.P. Uberuaga, D.A. Andersson, K.J. McClellan, C.R. Stanek, Band-gap engineering for removing shallow traps in rare-earth Lu$_3$Al$_5$O$_{12}$ garnet scintillators using Ga^{3+} doping, Phys. Rev. B 84 (2011) 081102.

[115] J. Ueda, Analysis of optoelectronic properties and development of new persistent phosphor in Ce^{3+}-doped garnet ceramics, J. Ceram. Soc. Jpn. 123 (2015) 1059–1064.

[116] Y.-C. Lin, P. Erhart, M. Bettinelli, N.C. George, S.F. Parker, M. Karlsson, Understanding the interactions between vibrational modes and excited state re-laxation in Y$_{3−x}$Ce$_x$Al$_5$O$_{12}$: design principles for phosphors based on 5d–4f tran-sitions, Chem. Mater. 30 (2018) 1865–1877.

[117] T. Lesniewski, S. Mahlik, K. Asami, J. Ueda, M. Grinberg, S. Tanabe, Comparison of quenching mechanisms in Gd$_3$Al$_{5-x}$Ga$_x$O$_{12}$:Ce^{3+} (x = 3 and 5) garnet phosphors by photocurrent excitation spectroscopy, PCCP 20 (2018) 18380–18390.

[118] J. Ueda, P. Dorenbos, A.J.J. Bos, A. Meijerink, S. Tanabe, Insight into the thermal quenching mechanism for Y$_3$Al$_5$O$_{12}$:Ce^{3+} through thermoluminescence excitation spectroscopy, J. Phys. Chem. C 119 (2015) 25003–25008.

[119] J. Ueda, M. Yagi, S. Tanabe, Editors' choice—investigation of luminescence and photoacoustic properties in Ce3+-doped Ln3Al5O12 (Ln = Lu, Y, Gd) garnet, ECS J. Solid. State Sci. Technol. 5 (2016) R219–R222.

[120] P. Dorenbos, Determining binding energies of valence-band electrons in insulators and semiconductors via lanthanide spectroscopy, Phys. Rev. B 87 (2013) 035118.

[121] P. Dorenbos, Modeling the chemical shift of lanthanide 4f electron binding en-ergies, Phys. Rev. B 85 (2012) 165107.

[122] P. Dorenbos, Ce^{3+} 5d-centroid shift and vacuum referred 4f-electron binding energies of all lanthanide impurities in 150 different compounds, J. Lumin. 135 (2013) 93–104.

[123] P. Dorenbos, Charge transfer bands in optical materials and related defect level location, Opt. Mater. 69 (2017) 8–22.

[124] V. Babin, M. Buryi, V. Chlan, Y. Fomichov, K. Kamada, V.V. Laguta, M. Nikl, J. Pejchal, H. Štěpánková, A. Yoshikawa, Y. Zagorodniy, S. Zazubovich, Influence of gallium content on Ga^{3+} position and photo- and thermally stimulated lumi-nescence in Ce^{3+}-doped multicomponent (Y,Lu)$_3$Ga$_x$Al$_{5-x}$O$_{12}$ garnets, J. Lumin. 200 (2018) 141–150.

[125] P. Dorenbos, E.G. Rogers, Vacuum referred binding energies of the lanthanides in transition metal oxide compounds, ECS J. Solid. State Sci. Technol. 3 (2014) R150–R158.

[126] J.B. Gruber, U.V. Valiev, G.W. Burdick, S.A. Rakhimov, M. Pokhrel, D.K. Sardar, Spectra, energy levels, and symmetry assignments for Stark components of Eu^{3+}(4f^6) in gadolinium gallium garnet (Gd$_3$Ga$_5$O$_{12}$), J. Lumin. 131 (2011) 1945–1952.

[127] K. Asami, J. Ueda, M. Shiraiwa, K. Fujii, M. Yashima, S. Tanabe, Redshift and thermal quenching of Ce^{3+} emission in (Gd, Y)$_3$(Al, Si)$_5$(O, N)$_{12}$ oxynitride garnet phosphors, Opt. Mater. 87 (2019) 117–121.

[128] P.Y. Jia, J. Lin, X.M. Han, M. Yu, Pechini sol–gel deposition and luminescence properties of Y$_3$Al$_{5-x}$Ga$_x$O$_{12}$:Ln^{3+} (Ln^{3+} = Eu^{3+}, Ce^{3+}, Tb^{3+}; 0 ≤ x ≤ 5) thin films, Thin Solid Films 483 (2005) 122–129.

[129] A. Katelnikovas, H. Bettentrup, D. Dutczak, A. Kareiva, T. Jüstel, On the correla-tion between the composition of Pr^{3+} doped garnet type materials and their photoluminescence properties, J. Lumin. 131 (2011) 2754–2761.

[130] D. Uhlich, P. Huppertz, D.U. Wiechert, T. Jüstel, Preparation and characterization of nanoscale lutetium aluminium garnet (LuAG) powders doped by Eu^{3+}, Opt. Mater. 29 (2007) 1505–1509.

[131] Z. Wang, M. Xu, W. Zhang, M. Yin, Synthesis and luminescent properties of nano-scale LuAG:RE^{3+} (Ce, Eu) phosphors prepared by co-precipitation method, J. Lumin. 122–123 (2007) 437–439.

[132] X. Liu, L. Zhu, L. Wang, C. Yu, J. Lin, Synthesis and luminescent properties of Lu$_3$Ga$_5$O$_{12}$: RE^{3+} (RE = Eu , Tb, and Pr) nanocrystalline phosphors via sol-gel process, J. Electrochem. Soc. 155 (2008) P21–P27.

[133] M. Liao, Z. Mu, Z. Shang, F. Wu, Z. Nie, Z. Zheng, X. Feng, Q. Zhang, J. Feng, D. Zhu, A red phosphor Mg$_3$Y$_2$Ge$_3$O$_{12}$: Bi^{3+}, Eu^{3+} with high brightness and ex-cellent thermal stability of luminescence for white light-emitting diodes, J. Lumin. 210 (2019) 202–209.